

VYSOKÉ UČENÍ TECHNICKÉ V BRNĚ

BRNO UNIVERSITY OF TECHNOLOGY

FAKULTA STROJNÍHO INŽENÝRSTVÍ

FACULTY OF MECHANICAL ENGINEERING

ÚSTAV FYZIKÁLNÍHO INŽENÝRSTVÍ

INSTITUTE OF PHYSICAL ENGINEERING

**SPEKTRÁLNÍ ANALÝZA A CHARAKTERIZACE
MAGNETICKÝCH ATOMŮ A STUDIUM
SUPRAVODIVÝCH VRSTEV POMOCÍ NÍZKOTEPLTNÍ
STM**

SPECTRAL ANALYZING AND CHARACTERIZATION OF MAGNETIC ATOMS AND INVESTIGATING
SUPERCONDUCTING FILMS IN LOW TEMPERATURE STM

DIPLOMOVÁ PRÁCE

MASTER'S THESIS

AUTOR PRÁCE

AUTHOR

Bc. Aleš Cahlík

VEDOUCÍ PRÁCE

SUPERVISOR

prof. RNDr. Tomáš Šikola, CSc.

BRNO 2016

Zadání diplomové práce

Ústav: Ústav fyzikálního inženýrství
Student: **Bc. Aleš Cahlík**
Studijní program: Aplikované vědy v inženýrství
Studijní obor: Fyzikální inženýrství a nanotechnologie
Vedoucí práce: **prof. RNDr. Tomáš Šikola, CSc.**
Akademický rok: 2015/16

Ředitel ústavu Vám v souladu se zákonem č. 111/1998 o vysokých školách a se Studijním a zkušebním řádem VUT v Brně určuje následující téma diplomové práce:

Spektrální analýza a charakterizace magnetických atomů a studium supravodivých vrstev pomocí nízkoteplotní STM

Stručná charakteristika problematiky úkolu:

Jedním z cílů současného výzkumu je zkombinovat znalosti atomového magnetismu na oddělovacích vrstvách se znalostmi nových supravodivých materiálů pro další studium souhry magnetismu a supravodivosti. Tato práce se především zaměřuje na první krok k tomuto cíli, a to materiálový výzkum vhodných systémů.

Další vývoj nanotechnologií pracujících na spinové bázi vyžaduje hlubší znalost magnetických vlastností atomových magnetů, především jejich magnetický moment a magnetická anisotropie. Nové možnosti na tomto poli mohou otevřít nedávné objevy dvoudimenzionálních materiálů, konkrétně dichalkogenidů přechodných kovů, a to například jejich využitím jako oddělovací vrstvy mezi magnetickými atomy a kovovými substráty.

Elektronické vlastnosti supravodivých materiálů se mění při dosažení limitu tenké vrstvy. Pro využití nových supravodivých materiálů, je důležité porozumět vlivu substrátu a tloušťky vrstvy na jejich elektronovou strukturu a vlastní supravodivost. Nízkoteplotní skenovací tunelovací mikroskopie/spektroskopie (LT-STM/STS) dovoluje simultánní charakterizaci elektronických a supravodivých vlastností takových vrstev.

Cíle diplomové práce:

Rekonstrukce a přestavba 4K Omicron LT-STM s cílem provádět STS při teplotách kapalného helia s dostatečným energiovým rozlišením pro supravodivá měření.

Studium magnetických atomů na jednovrstevných dichalkogenidech přechodných kovů pomocí X-ray magnetic circular dichroism (XMCD).

- Studium magnetického momentu a anisotropie Co atomů na WS₂ na MoS₂.
- Studium role spin orbitální vazby při určování magnetické anisotropie Co atomů.
- Studium efektu oddělovací vrstvy na vazbu mezi magnetickým momentem Co atomů a substrátem (Au(111)).

Studium růstu tenkých supravodivých vrstev na kovových substrátech pomocí 4K STM/STS.

- Výzkum změny supravodivé mezery v limitě tenké vrstvy v porovnání s objemem.
- Výzkum elektronové struktury tenké vrstvy a role substrátu, jakož i vznik vázaných kvantových stavů.

Seznam literatury:

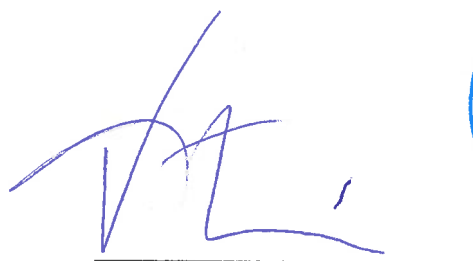
MIWA, Jill A., Soren ULSTRUP, Signe G. SORENSEN, Maciej DENDZIK, Antonija Grubišić ČABO, Marco BIANCHI, Jeppe Vang LAURITSEN a Philip HOFMANN. Electronic Structure of Epitaxial Single-Layer MoS₂ [online]. 2014 [cit. 2015-11-23]. DOI: 10.1103/PhysRevLett.114.046802

EOM, Daejin, S. QIN, M.-Y. CHOU a C.K. SHIH. Persistent Superconductivity in Ultrathin Pb Films: A Scanning Tunneling Spectroscopy Study [online]. [cit. 2015-11-23]. DOI: <http://dx.doi.org/10.1103/PhysRevLett.96.027005>.

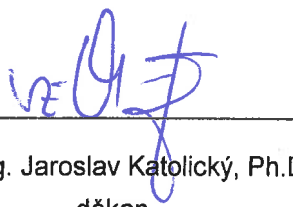
NADJ-PERGE, Stevan, Ilya K. DROZDOV, Jian LI, Hua CHEN, Sangjun JEON, Jungpil SEO, Allan H. MACDONALD, B. Andrei BERNEVIG a Ali YAZDANI. Observation of Majorana Fermions in Ferromagnetic Atomic Chains on a Superconductor [online]. 2014 [cit. 2015-11-23]. DOI: 10.1126/science.1259327.

Termín odevzdání diplomové práce je stanoven časovým plánem akademického roku 2015/16.

V Brně, dne 24. 11. 2015



prof. RNDr. Tomáš Šíkola, CSc.
ředitel ústavu



doc. Ing. Jaroslav Katolický, Ph.D.
děkan

Abstrakt

Tato diplomová práce se dělí na dva tématické podcelky. První tématický podcelek se věnuje renovaci nízkoteplotního STM zařízení od firmy Omicron a jeho následnému využití pro studium preparace supravodivých-magnetických rozhraní. Nejprve je zde ukázána příprava vhodných kovových substrátů, konkrétně W(110) a Ir(111). Dále práce ukazuje výsledky přípravy tenkých železných vrstev na Ir(111). Poslední sekce se zabývá studiem růstu vanadia jak na čistém Ir(111) tak na zmíněném systému Fe-Ir(111). Druhý tématický podcelek se zabývá magnetismem kobaltových atomů na jednovrstevném dichalkogenidu WS₂. Jedná se především o studium jejich magnetického momentu a anisotropie pomocí X-ray magnetic circular dichroism (XMCD).

Summary

This work is divided in two thematic parts. The first part shows a refurbishment of a Omicron low temperature STM set-up and its utilization for preparation of superconducting-magnetic interfaces. First, a cleaning procedure of suitable metallic substrates, specifically W(110) and Ir(111), is shown. It is followed by results of iron monolayer deposition on Ir(111) (Fe-Ir(111) interface). The last section deals with study of vanadium growth on pure Ir(111) substrate as well as on mentioned Fe-Ir(111) interface. The second thematic part deals with magnetism of cobalt atoms on a monolayer metal dichalcogenide WS₂. It focuses primarily on studying their magnetic moment and magnetic anisotropy using X-ray magnetic circular dichroism (XMCD).

Klíčová slova

nízkoteplotní skenovací tunelovací mikroskopie, LT-STM, skenovací tunelovací spektroskopie, STS, kryogenika, UHV supravodivost, magnetismus, vanad, nanoskyrmion, Ir(111), W(110), kobalt, dichalkogenidy

Keywords

low temperature scanning tunneling microscopy, LT-STM, scanning tunneling spectroscopy, STS, cryogenics, UHV, superconductivity, magnetism, vanadium, nanoskyrmion, Ir(111), W(110), cobalt, dichalcogenides,

Cahlík, ALEŠ. *Spektrální analýza a charakterizace magnetických atomů a studium supravodivých vrstev pomocí nízkoteplotní STM*. Brno, 2016. 57 s. Diplomová práce. Vysoké učení technické v Brně. Fakulta strojního inženýrství. Vedoucí práce Tomáš ŠIKOLA.

Prohlašuji, že jsem diplomovou práci Spektrální analýza a charakterizace magnetických atomů a studium supravodivých vrstev pomocí nízkoteplotní STM vypracoval samostatně pod vedením prof. RNDr. Tomáše Šikoly, CSc. s použitím materiálů uvedených v seznamu literatury.

Bc. Aleš Čahlík

Děkuji Prof. Dr. Alexandru Khajetooriansovi za umožnění a vedení mé stáže v laboratořích Radboud University of Nijmegen a na synchrotronu Diamond Light Source. Děkuji všem členům SPM skupiny na Radboud University of Nijmegen za veškerou pomoc během mé práce, především Judith Donner, MA za její podporu a kritický náhled při psaní textu. Děkuji Dr. Janu Honolkovi, Mgr. Martinu Vondráčkovi a Dr. Charlotte Sanders za jejich trpělivé vysvětlování během beamtime na Diamond Light Source. Děkuji Diamond Light Source za přístup k měření na beamline I06, který přispěl k výsledkům prezentovaným v této práci. Děkuji své rodině a všem blízkým, za jejich podporu v průběhu celého mého studia. Děkuji svému vedoucímu prof. RNDr. Tomáši Šikolovi, CSc. za vedení mé diplomové práce.

I would like to thank Prof. Dr. Alexander Khajetoorians for leading and supporting my internship at Radboud University of Nijmegen and at Diamond Light Source. I owe thanks to all members of the SPM group at Radboud University of Nijmegen for all their help, in the first place Judith Donner, MA for her support and critical comments during the writing. I would like to thank Dr. Jan Honolka, Mgr. Martin Vondráček and Dr. Charlotte Sanders for patient explanations during the beamtime at Diamond Light Source. I thank Diamond Light Source for access to beamline I06 that contributed to the results presented here. Special thanks go to my family and all my close friends, for their support during my whole study period. I would like to thank prof. RNDr. Tomáš Šikola, CSc. for supervising my thesis.

Bc. Aleš Cahlík

Contents

Introduction	1
1. Experimental LT-STM set-up and its modifications	3
1.1. Theory of Scanning Tunneling Microscopy	3
1.1.1. Scanning Tunneling Microscopy	3
Fundamentals of tunneling	3
Scanning mode	5
1.1.2. Scanning Tunneling Spectroscopy	5
Differential conductance	6
Technical realization	6
Energy resolution	7
Differential conductance mapping	8
1.2. Theory of Superconductivity	8
1.3. Experimental set-up	10
1.3.1. Omicron LT-STM	11
Load-lock chamber	11
Preparation chamber	12
LT-STM chamber	12
1.4. Refurbishment of the experimental set-up	14
1.4.1. Drawbacks of the original design	14
1.4.2. Modifications	14
Shielding improvement	14
Wiring improvement	15
Electronics and control unit change	17
1.5. Results of the refurbishment and test measurements	17
1.5.1. Cryostat standing time change	17
1.5.2. STM and STS test measurements	17
Au(111)	18
Pb(111)	19
2. Preparation of superconducting-magnetic interfaces	23
2.1. Choice of the material	23
2.1.1. Substrate and magnetic film	24
Majorana fermions observation	24
2.1.2. Superconducting film	24
2.2. Substrate preparation	25
2.2.1. W(110) preparation	25
Oxygen reconstruction	26

Carbon reconstruction	27
2.2.2. Ir(111) preparation	28
2.3. Growth of Fe on Ir(111)	30
2.4. Growth of V on Ir(111)	33
2.5. Growth of V on Fe-Ir(111)	36
3. Magnetism of Co atoms on WS₂	43
3.1. X-ray circular magnetic dichroism (XMCD)	43
3.2. Motivation and sample preparation	45
3.2.1. WS ₂	45
3.2.2. Sample preparation – Co on WS ₂	46
3.3. First results	46
Summary and outlook	49
References	51
List of used abbreviations	57

Introduction

A lot of different aspects of nanoscale magnetism have been studied in the past, like e.g. current induced magnetization switching of superparamagnetic islands [1], nanoskyrmion lattices in iron thin films [2, 3] or atom-by-atom engineering of tailored nanomagnets [4]. Moreover the growth of thin superconducting materials [5, 6] has been as well a subject of great scientific and technological importance. The ultimate goal of this research is to combine the knowledge on magnetic layers and single magnetic atoms with superconducting materials to look at the interplay between magnetism and superconductivity at the atomic scale. This work aims at the first steps toward this goal, namely an investigation of suitable material systems. Therefore this thesis is divided into two thematic parts:

1. LT-STM study on preparation of superconducting-magnetic interfaces
(Chapter 1 and Chapter 2)
2. XMCD study on magnetic anisotropy of single Co atoms on $\text{WS}_2/\text{Au}(111)$
(Chapter 3)

LT-STM The first thematic part focuses on the preparation of stable superconducting-magnetic interfaces in the low temperature scanning tunneling microscope (LT-STM) experimental set-up. Such interfaces could create proper conditions to study new physical phenomena, like e.g. the observation of Majorana fermions in ferromagnetic atomic chains on a superconductor [7]. LT-STM allows for a simultaneous characterization of the electronic and superconducting properties of nanoscale interfaces with atomic resolution.

Chapter 1 provides the theoretical fundamentals for scanning tunneling microscopy and superconductivity in solids. Then, the Omicron LT-STM set-up utilized during the course of this work is described. The main part of this chapter details the refurbishment and rebuilding of the LT-STM experimental set-up with the aim to improve its user-friendliness, measurement stability, energy resolution and cryostat standing time.

Chapter 2 presents a study on the growth of superconducting vanadium films on metallic substrates. The first step was to adapt a previously reported procedure [8–10] for preparation of atomically clean $\text{W}(110)$ and $\text{Ir}(111)$ substrates in our experimental set-up. The second step was to reproduce the growth of single-layer iron films on the $\text{Ir}(111)$ substrate ($\text{Fe}/\text{Ir}(111)$) [3]. On contrary to this, the growth of a thin vanadium films on $\text{Ir}(111)$ and $\text{Fe}/\text{Ir}(111)$ was an unexplored field. The aim was to find the right growth parameters to prepare atomically flat continuous films of vanadium, without alloying with the substrates or big lattice mismatch.

XMCD The further development of nanoscale spin-based technologies requires a deeper knowledge of the magnetic properties such as the magnetic anisotropy of atom-scale magnets. For instance, Gambardella et *al.* [11] showed a study of giant magnetic anisotropy of

INTRODUCTION

single cobalt atoms on Pt(111). The recent emergence of two-dimensional layered materials, in particular the transition metal dichalcogenides, can open a new route in this field by using them as a separation layer between magnetic adatoms and metallic substrates.

Chapter 3 demonstrate first results of X-ray magnetic circular dichroism (XMCD) data measured on single cobalt atoms deposited on WS₂/Au(111) during the beam time at Diamond Light Source facility [12].

1. Experimental LT-STM set-up and its modifications

In the first section of this chapter, Scanning Tunneling Microscopy (STM) is introduced. The second section presents the fundamentals of Superconductivity. The third section focuses on the LT-STM experimental set-up, that was utilized during the course of this work. The last section then describes all the necessary modifications, that have been carried out on the system to improve its performance.

1.1. Theory of Scanning Tunneling Microscopy

In the first part of this section, fundamentals of the tunneling theory and STM measuring modes are presented. Afterwards, a method for obtaining differential conductance spectra, namely scanning tunneling spectroscopy (STS), is introduced.

1.1.1. Scanning Tunneling Microscopy

Since its introduction by Binnig and Rohrer in 1982 [13], the Nobel prize awarded invention of scanning tunneling microscopy (STM) provides the researchers with a powerful tool for their work in the field of nanotechnology and surface science. By taking advantage of the quantum-mechanical tunneling effect, the STM operation principle is based on moving a sharp tip in the vicinity of a surface. Simultaneously, a measurement of various surface properties is performed with a spatial resolution on the nanometer or even atomic scale. The ability of precise local probing gives STM a major advantage over other surface sensitive techniques that provide averaged information over a certain surface area such as LEED, XPS, XAS, ARPES and others. [14]

Fundamentals of tunneling

In contrast to classical mechanics, a quantum mechanical approach allows electrons to penetrate into a barrier region with higher energy than its own. Within the barrier, the probability density decays exponentially with the distance from the barrier boundary. If we consider the tip and the sample as two separated metal electrodes and the vacuum between them as a potential barrier, bringing the electrodes close to each other (typically in order of units of Å) will increase the probability of successful electron tunneling through the potential barrier. As the probability of tunneling in this case is identical for both directions, to establish a unidirectional current, a bias voltage has to be applied between the electrodes.

Long before the STM invention, **Bardeen** [15] developed the first theoretical approach to describe the tunneling phenomena in solids by considering a metal-insulator-metal

1. EXPERIMENTAL LT-STM SET-UP AND ITS MODIFICATIONS

junction. His approach was later successfully used in the case of the STM theory. Dealing with the tip and the sample as with the two electrodes biased by a voltage V_{bias} and separated by a vacuum potential barrier of width d (at $T = 0$ K), the tunneling current I between them can be written as [16]:

$$I = \frac{4\pi e}{\hbar} \int_0^{eV_{\text{bias}}} \varrho_{\text{tip}}(\varepsilon - eV_{\text{bias}}) \varrho_{\text{sample}}(\varepsilon) T(\varepsilon, V_{\text{bias}}, d) d\varepsilon, \quad (1.1)$$

where ε is the energy relative to the Fermi energy of the sample, ϱ_{tip} is the tip density of states, ϱ_{sample} the sample density of states and T the transmission factor. The transmission factor indicates the probability of the successful electron tunneling at the certain energy ε . In the Wentzel-Kramers-Brillouin semi-classical approximation for one dimension, the transmission factor in Eq.1.1 can be expressed by the following formula [16, 17]:

$$T(\varepsilon, V_{\text{bias}}, d) \propto \exp \left[-2d \sqrt{\frac{2m}{\hbar^2} \left(\frac{\Phi_{\text{tip}} + \Phi_{\text{sample}}}{2} + \frac{eV_{\text{bias}}}{2} - \varepsilon \right)} \right]. \quad (1.2)$$

A schematic energy level diagram of the one-dimensional tunneling junction is presented in Fig.1.1, where the tip and the sample are separated by the distance d at temperature $T = 0$ K. The density of states (DOS) ϱ_{tip} and ϱ_{sample} are indicated by a vertical curves with filled states up to the Fermi energy (E_{F}). The height of the tunneling barrier is determined by the work functions Φ , which are characteristic for each material and define the energy, that is needed to extract an electron from the material to the vacuum level. By applying a bias voltage V_{bias} between the electrodes, their Fermi levels are shifted by $\Delta E_{\text{F}} = eV_{\text{bias}}$. This enables unidirectional tunneling of electrons from the tip occupied states into the sample unoccupied states or vice versa (depending on the bias sign) through the potential barrier (blue arrows). Due to the exponential decay of the transmission factor for lower electron energies, the tunneling is most probable for the states near the E_{F} – indicated by the decreasing arrow size.

For the real STM measurements, however, the Bardeen model for planar electrodes is not sufficient since the tip shape, the tip wave functions and tip density of states are unknown. In the **Tersoff-Hamann** approximation [18] only a very small bias voltage is considered, making the tunneling possible only at E_{F} and thus independent of the energy. Moreover, the tip is approximated as a mathematical point with the position r_{t} above the sample and all the complex tip properties are removed. Tersoff and Hamann also showed, that within this approximation, the tip can be also viewed as single atom represented by simple s-wavefunction with the effective center of curvature at r_{t} . Within this approach, the tunneling current depends only on ϱ_{sample} at the center of the tip curvature r_{t} [16, 19]:

$$I \propto \varrho_{\text{sample}}(E_{\text{F}}, r_{\text{t}}), \quad (1.3)$$

Therefore, the STM tip probes the sample local density of states (LDOS) near Fermi energy E_{F} directly at the effective center of curvature r_{t} where the tip is located. And since the wavefunction of the sample decay exponentially with the distance on scale of a few \AA , it can be shown, that a majority of the tunneling current goes through the atom closest to the sample surface [19].

Please note, that in all presented theoretical descriptions were the Fermi Functions of the tip and the sample considered as a step functions ($T = 0$ K). However, for the finite

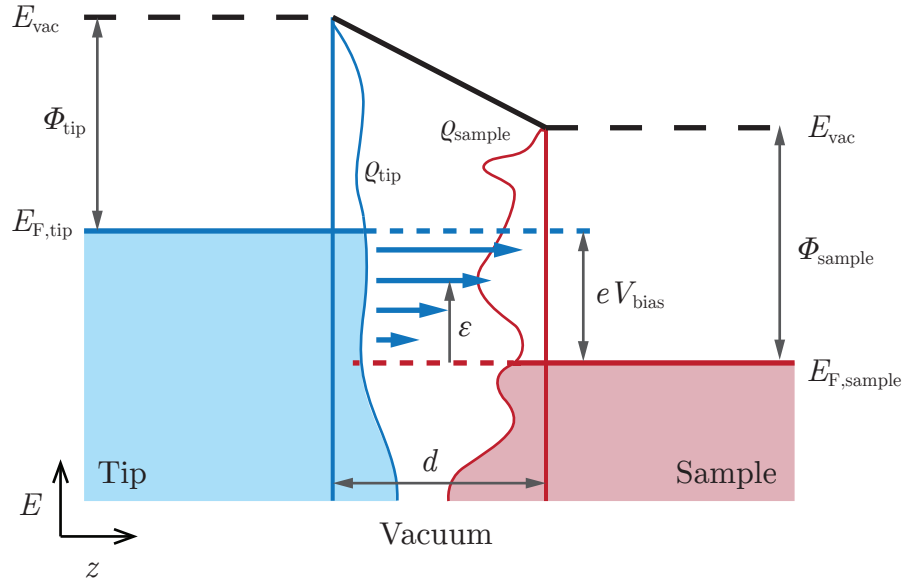


Figure 1.1: The energy level diagram of the one dimensional tunneling junction. The tunneling current is established by applying a bias voltage V_{bias} that enables the electrons to tunnel from the occupied states of the tip into the unoccupied states of the sample. Due to the varying transmission factor, the electrons near the tip E_F have a higher probability of a successful tunneling.

temperatures and especially when a good energy resolution is needed, the broadening of the Fermi levels has to be taken into account.

Scanning mode

The usual STM design utilizes a piezoelectric actuator to approach the tip and scan it over the surface [13, 16, 20, 21]. By applying a voltage on the the piezo element, it can be stretched along desired direction. The actuator has usually a three degrees of freedom and besides the tip-sample distance regulation in the z direction, it also performs the scanning along the x and y axes. In principle, there are two modes, that can be utilized - constant current mode and constant height mode. During the course of this work, a constant current mode have been used to measure all the presented topography data.

In constant current mode, a constant current value is maintained during the scanning of the surface. This is done by adjusting the tip position in order to keep the tip-sample distance also constant. The tip-sample distance regulation is operated via a feedback loop, that measures the tunneling current and stretches the piezo actuator accordingly by applying a voltage to its electrodes. The resulting topography image is then reconstructed from the stretch, respective voltage, amplitude of the actuator in z direction for each point of the scan.

1.1.2. Scanning Tunneling Spectroscopy

As shown, STM provides an effective tool to study the local properties of the investigated surfaces at atomic scale. This subsection presents a technique to measure the energy dependence of the local density of states of the surface – the so-called scanning tunneling spectroscopy (STS).

Differential conductance

If the tip is positioned above the surface in a fixed distance d , a small increase of the bias voltage dV will increase the tunneling current by dI , because a new empty state of the sample becomes available. As can be seen in Fig.1.1 and Eq.1.2, the tunneling electrons, that contribute to this new current increase, have the lowest apparent barrier height and thus also the highest transmission coefficient. To realise the basic principle of STS in the first approach, the tip density of states ϱ_{tip} and transmission factor $T(\varepsilon, V_{\text{bias}}, d)$ can be approximated as constant with respect to energy (we consider only a small bias voltage). By considering these approximations, we can differentiate the Eq.1.1 and with the help of Leibniz integral rule, we can obtain [16, 22]:

$$\frac{dI}{dV} \approx C \varrho_{\text{sample}}[e(V + dV)]T[e(V + dV), V + dV], \quad (1.4)$$

where we substituted for energy $\varepsilon = e(V + dV)$. It is the energy of a newly available sample states (appearing under the blue dashed line in Fig.1.1), when the voltage is increased. From this approximation we can see, that the differential conductance signal is proportional to the sample density of states. Nevertheless, it is necessary to keep in mind for the real STS measurements, that the ϱ_{tip} is unknown and can not be always approximated as constant. Because this fact can significantly influence the shape of the spectral curve, it is always necessary to reproduce the measured data with different tip shapes or check the tip quality on a material with well studied characteristic spectra for comparison.

Technical realization

To investigate the sample density of states and obtain the differential conductance spectra presented in this thesis, a constant height spectroscopy mode was used. First, the tip is placed over a desired spot on the surface with a defined bias voltage and tunneling current. This set-point corresponds to a certain tip-sample distance, which is stabilized and fixed by switching off the feedback loop. Afterwards, the bias voltage is swept over a defined range (the bias voltage in V corresponds to the energy of eV) and the dI/dV signal can be recorded. There are two main ways used to measure the differential conductance spectrum - numerical differentiation of the $I(V)$ curve and the lock-in technique.

Numerical differentiation The simplest way, without necessity of any additional electronics, is to record the $I(V)$ signal and differentiate it numerically after the measurement. Besides the asset of short sweeping time, that reduces the influence of thermal drift, this technique usually lacks the sufficient signal-to-noise ratio. This applies especially for the higher tunneling currents, respective energies. Unfavourable signal-to-noise ratio is caused mainly by the fact, that the noise in the tunneling current appearing at all frequencies, is amplified together with the current signal. For this reason, we utilized during the course of this work a following technique to solve the signal-to-noise ratio problem.

Lock-in technique The second and the most convenient technique for measuring the dI/dV signal is implementation of lock-in amplifier [23, 24], a device that solves the problem of recovering the signal even if its broadband noise is much larger.

A comparatively small AC reference signal $V_{\text{mod}} \cos \omega_{\text{mod}} t$ with frequencies in the order of kHz is added to the DC bias voltage. This leads to an oscillating signal in the tunneling current around its DC component. This signal is fed into a lock-in amplifier device, that

is able to extract only the oscillating signal amplitude with frequency ω_{mod} and suppress all other signals (including the noise). It is possible due to the fact, that sinusoidal functions are orthogonal. It means, that when we integrate a product of two sinusoidal functions with frequencies ω_1 and ω_2 , the result is non-zero only in the case of $\omega_1 = \omega_2$ and consistent phase of the two signals. The lock-in integrates (time averages over time period) the tunneling current with the reference signal and obtains the amplitude of the oscillating component in the tunneling current. For a successful signal extraction, the phase difference between the oscillating current and the reference signal has to be zero and the interval for the time averaging sufficiently long (several periods of the two signals).

The principle of this technique is indicated for the hypothetical $I(V)$ curve in Fig.1.2. The two different amplitudes $I_{\text{mod},1}$ and $I_{\text{mod},2}$ are obtained for the same modulation voltage V_{mod} at different energies. It can be deduced that the resulting oscillating signal amplitude I_{mod} is proportional to the slope of the curve $I(V)$ and thus to dI/dV . [16]

The voltage modulation amplitude V_{mod} and its frequency ω_{mod} can be manually selected by user on the lock-in amplifier.

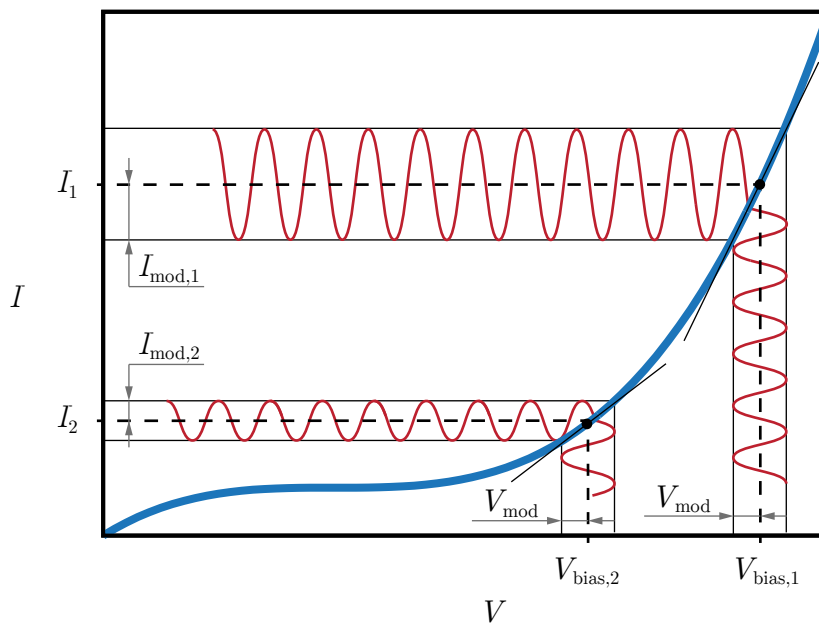


Figure 1.2: The basic principle of implementing the lock-in technique for measuring the differential conductance dI/dV . From the hypothetical $I(V)$ curve, it can be inferred that the amplitude I_{mod} of the oscillating component of the tunneling current is proportional to the slope of the $I(V)$ curve and thus to the differential conductance dI/dV .

Energy resolution

For distinguishing subtle features in the order of mV in the differential conductance spectra, a good energy resolution is crucial. The resolution can be affected mainly by the temperature, the modulation voltage of the lock-in amplifier and the noise coupled to the signal.

In real measurements at finite temperatures above the $T = 0$ K, a temperature broadening of the Fermi function has to be taken into account. The transmission factor in this case can be treated as constant, because the Fermi energy broadening applies only

1. EXPERIMENTAL LT-STM SET-UP AND ITS MODIFICATIONS

in a small energy range of $k_B T$. In this case, the density of states has to be convoluted with a differentiated thermally broadened Fermi function $f(\varepsilon - eV, T)$ and the differential conductance is then proportional to [16, 25]:

$$\frac{dI}{dV} \approx C \int_{-\infty}^{\infty} \frac{\partial f(\varepsilon - eV, T)}{\partial V} \rho_{\text{sample}}(\varepsilon) d\varepsilon. \quad (1.5)$$

As can be seen in Fig.1.2, the accuracy of the resulting dI/dV signal is dependent on the modulation voltage amplitude. This fact also contribute to the energy resolution of the lock-in technique. Therefore it is necessary to choose the modulation voltage, comparatively smaller than the energy scale of the investigated feature. [25]

The noise, originating from both vibrational and electronic sources, can be coupled to the tunneling signal. To attenuate its influence, various mechanical damping systems are included in the STM design and all the electronics have to be properly shielded and grounded [21]. However, the problem of noise in STS measurements can be removed by using the lock-in technique, that suppresses all the signals on different frequency then ω_{mod} . For this reason, it is desirable to chose a modulation frequency ω_{mod} , that does not have any significant broadband noise peak in its vicinity.

Differential conductance mapping

The ability of probing the local density of states on the sample surface above a specified point can be expanded by a spectroscopy mapping technique. In this mode, a spatial map of the local density of states (LDOS) at a desired energy (bias voltage) can be measured simultaneously with a slow constant current topography image. This is realized by recording the dI/dV signal obtained from the modulated tunneling current by the lock-in amplifier at every point of the scan. It is usually performed at energy corresponding to the particular feature in differential conductance spectra to acquire additional information about the spatial distribution of the surface electronic structure.

1.2. Theory of Superconductivity

Superconductivity was first discovered by H.K. Onnes in 1911 [26] as a consequence his another famous accomplishment – the first successful helium liquification in 1908 [27]. He observed an unexpected electrical resistance drop in the sample of solid mercury when cooled down to LHe temperature around 4.2 K. Following his discovery, large numbers of elements, alloys and compounds were reported to exhibit superconductivity after cooling down under a certain critical temperature T_C , which is characteristic for each material. The highest $T_C = 9.3$ K among pure elements has Niobium [28].

Another interesting discovery of superconducting behaviour was made by Meissner and Ochsenfeld in 1933 [29]. They found out that when a superconductor is exposed to a weak magnetic field and cooled down below its T_C , the field is expelled outside the superconductor volume in spite of expectations of a classical Maxwell's theory. The annihilation of the magnetic field in a superconductor is a consequence of its internal loop currents, induced by the change of magnetic flux. These currents flow without resistance and generate a field in the opposite direction to the applied field, thus completely cancelling the field inside. [30]

Whereas the weak magnetic field is expelled from a superconducting material, there is a critical magnetic field H_C value above which the superconductivity is completely

destroyed. Such suppression of superconductivity can happen in two ways and the superconductors are accordingly divided into type-I and type-II superconductors. In contrast to the type-I superconductors, which have only one value of critical field H_C , type-II superconductors exhibit two critical field values - H_{C1} and H_{C2} . Above H_{C2} , the superconductivity is completely destroyed as in the case of type-I, but in the interval between H_{C1} and H_{C2} , a so called mixed or Shubnikov phase occurs and the field can penetrate into the material in a special spatial arrangement while preserving the superconductivity [31]. The phase diagrams of the field changes for both types are shown in the Fig. 1.3a.

The so-called conventional superconductors, that were investigated in the course of this thesis, can be described by a theory developed by Bardeen, Cooper and Schrieffer in 1957 [32]. The theory describes a phonon mediated attraction between two electrons in a lattice of ion cores at low temperatures that can overcome the Coulomb repulsion. Electrons in such bound state are called Cooper pairs and consist of particles with opposite momentum and spin. These pairs act like bosons and can condensate to the same quantum state at low temperatures forming a Bose condensate, that conducts electric current without resistance. A measure of the density of the Cooper pairs in the superconductor is called a coherence length and has values typically in the order of many interatomic distances [33].

Cooper pairs can be destroyed by thermal or electromagnetic excitation. According to the BSC theory, the excited electrons then occupy states with higher energy and are called elementary excitations or quasiparticles. The ground energy state of Cooper pairs is separated from the excited quasiparticle states by an energy gap Δ . In order to destroy a Cooper pair, an energy of at least 2Δ is needed (usually in the energy range of meV) [31].

The density of states of quasiparticles in a superconductor resulting from the BSC theory is dependent on the energy E as [34]:

$$\varrho_{\text{BSC}} = \begin{cases} \varrho_{\text{N}} \frac{|E|}{\sqrt{E^2 - \Delta^2}}, & E > \Delta \\ 0, & E < \Delta \end{cases} \quad (1.6)$$

where ϱ_{N} is the DOS in the normal conducting state and following the BSC theory is considered as constant. Because the quasiparticles can recombine back into the SC state or be scattered to a different quasiparticle state, their lifetime is not infinite. This results into a lifetime broadening of the energy gap as was shown by Dynes *et al.* [35]:

$$\varrho_{\Gamma} = \frac{|E| - i\Gamma}{\sqrt{(E - i\Gamma)^2 - \Delta^2}}, \quad (1.7)$$

where Γ is the quasiparticle lifetime parameter.

At finite temperatures, the SC energy gap is as well broadened due to the thermal excitations of quasiparticles from the ground state. At the critical temperature, all the electrons are in the excited quasiparticle state and the energy gap completely vanishes [31].

Fig.1.3b shows plots of quasiparticle density of states of SC energy gap $\Delta = 2.2$ meV for the mentioned cases. The green line shows the $T = 0$ K case without lifetime broadening according to Eq.1.6, the red line represents the $T = 0$ K case with a lifetime broadening $\Gamma = 0.1$ meV according to Eq.1.7 and the blue line shows the thermal broadened case for $T = 4.3$ K.

1. EXPERIMENTAL LT-STM SET-UP AND ITS MODIFICATIONS

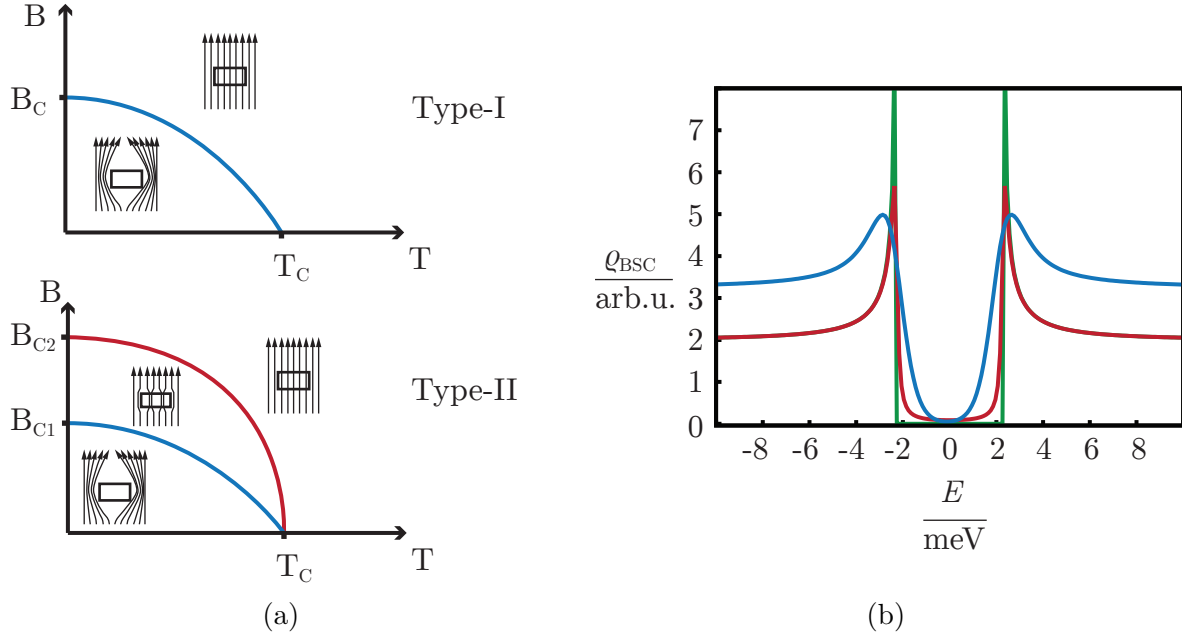


Figure 1.3: (a) Phase diagrams of Type-I and Type-II superconductors. When cooled below T_C , field is expelled out of the volume below B_C , respectively B_{C1} . Above B_C , respectively B_{C2} , the field penetrates into the volume. For Type-II superconductors a Shubnikov phase occurs between B_{C1} and B_{C2} . (b) DOS of quasiparticles according to Eq.1.6 for $T = 0$ K (green line), according to Eq.1.7 for $T = 0$ K and $\Gamma = 0.1$ meV (red line), according to Eq.1.7 and convoluted with thermally broadened Fermi function (blue line). The quasiparticle peaks do not diverge for both broadened DOS cases. ($\Delta = 2.2$ meV)

1.3. Experimental set-up

This section describes the experimental system which was utilized during the work presented in this thesis. It is a low temperature (LT) ultra high vacuum (UHV) STM made by Omicron NanoTechnology [36]. Necessary modifications of the system made during the course of this work are detailed in the next section.

Performing measurements in ultra high vacuum at low temperatures is essential for the experiments described in this work because of stable and clean environment conditions. Moreover, to study superconductivity one has to reach the critical temperature (T_c) of the material.

Low temperatures create a time-stable condition of the surface by reducing a mobility of atoms and the low thermal drift of the sample. In combination with low thermal drift of the scanner piezo, the tip can sustain a fixed position above the desired spot on the sample for hours.

Beyond that, since the tunnelling effect depends strongly on the tip-sample distance, less diffusion on the apex of the tip helps to stabilize the tunnelling itself. For the same reason, it is also essential to isolate the system from any external mechanical vibrations that could affect the tunnelling distance.

As mentioned, the ultra high vacuum conditions maintain investigated surface clean of any impurities during the preparation and scanning, that could affect the experimental results strongly.

And last but not at least, as the tunnelling current is very low (usually in the order of pA), getting a high lateral and energy resolution requires proper electromagnetic shielding of the conducted signals and state of the art electronics with excellent signal-to-noise ratio.

1.3.1. Omicron LT-STM

The Omicron LT-STM described here belongs to the first generation of Omicron low temperature microscopes [36]. Its simplified schematic drawing with sample transfer scheme is shown in Fig.1.8. The set-up consists of three main chambers described in the following subsections - load-lock chamber, preparation chamber and LT-STM chamber. They are connected by gate valves and so their environments can be controlled separately.

The whole chamber system is attached to the supporting frame that rests on the pneumatic suspension legs (Newport) with resonant frequencies below 2 Hz. Their purpose is to isolate the system from any mechanical disturbance caused by building vibrations and acoustic waves. There is a second mechanical vibration isolation system directly on the STM stage, that will be described in subsection 1.3.1.

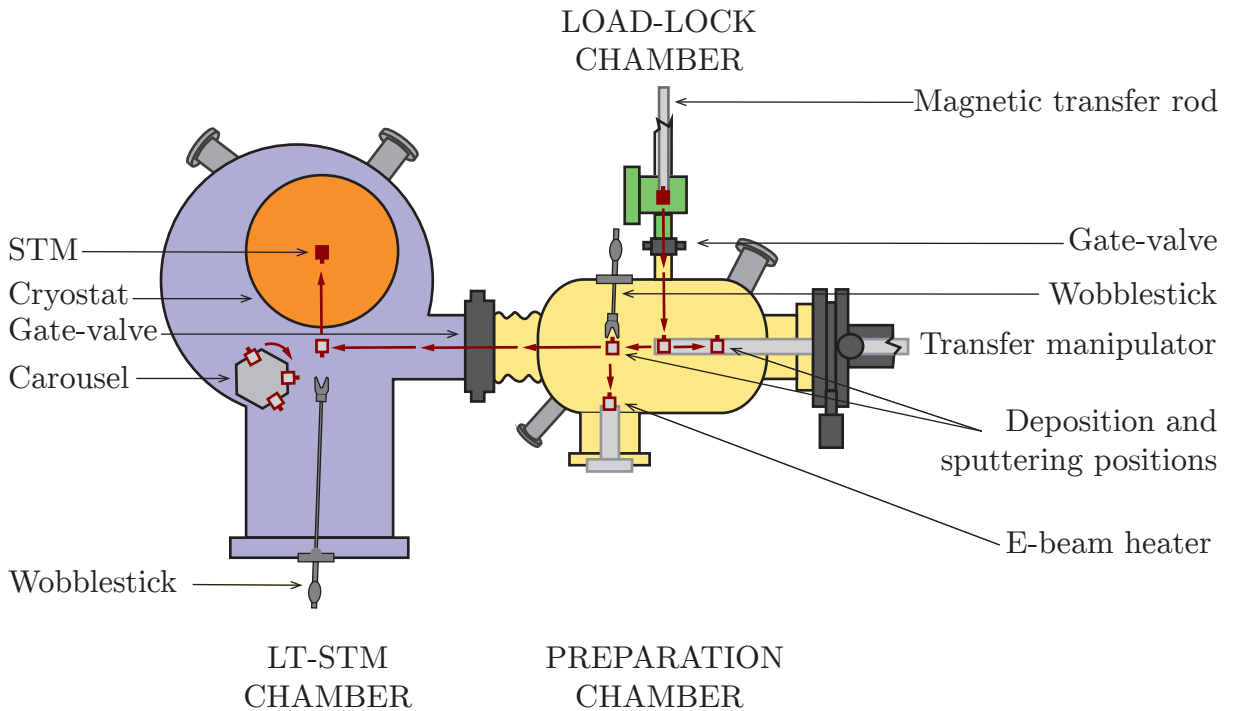


Figure 1.4: Schematic drawing of the experimental set-up of the Omicron UHV LT-STM and the sample transfer line. Load-lock chamber – green. Preparation chamber – yellow. LT-STM chamber – blue.

Load-lock chamber

To introduce a sample into the system, a small fast entry load-lock chamber is used. It can be separated and pumped independently by a turbo molecular pump and it can also be easily vented. For regular use the load-lock chamber is not baked after venting and reaches the base pressure in the upper $10 \cdot 10^{-8}$ mbar regime. However, for inserting the samples into the preparation chamber during normal operation, a pressure in the range of $10 \cdot 10^{-6}$ mbar is sufficient and can be reached within only 30 minutes. The transfer to the preparation chamber is done via the magnetic transfer rod.

1. EXPERIMENTAL LT-STM SET-UP AND ITS MODIFICATIONS

Preparation chamber

All the sample preparation steps take place in this chamber. The pumping system consists of an ion getter pump combined with a titanium sublimation pump which reaches the base pressure in the range of the upper $10 \cdot 10^{-11}$ mbar, but for the baking of the system and the sample preparation in gas atmospheres above $10 \cdot 10^{-8}$ mbar, the preparation chamber can be also pumped directly by the turbo molecular pump.

From the load-lock chamber the sample is placed on the long travel transfer manipulator with four degrees of freedom (x, y, z, φ). Samples can be then transferred into the STM chamber or moved to the desired positions for the sample processing within the preparation chamber with millimetre accuracy. It is possible to define and control the sample temperature when it is placed on the manipulator head with a thermocouple temperature reading. It can be cooled with by a flow cryostat with either liquid nitrogen or liquid helium or on the contrary heated up to 500°C by resistive heating.

To anneal the samples above 500°C , the chamber is equipped with an electron bombardment heater. It comprises the sample stage with a tungsten filament underneath it. By applying a high voltage up to 1 kV between the filament and the sample plate, the electrons emitted from the filament are accelerated towards the plate, heating it due to a high concentration and power of impacting electrons. For sample annealing at different gas atmospheres (O_2 in the case of this work), a needle valve is used to introduce desired amount of gas into the chamber. Furthermore, the sample surface can be cleaned by an ion bombardment from an argon sputter gun.

And once the substrate surface is clean, various metals can be deposited on top of it by using one of the six electron beam evaporators, that work on the same principle as the electron bombardment heater – heating the metallic rod by electron bombardment and evaporating it onto the sample.

LT-STM chamber

The LT-STM chamber houses the main analytical tool of the whole system - cryostat with the LT-STM. The vacuum generation is ensured by an ion getter pump and a titanium sublimation pump like in the preparation chamber. Moreover, the cryostat and all its connected parts, when cooled, adsorbs the atoms of the residual gases and acts as a cryogenic pump, further improving the vacuum in the chamber to lower $10 \cdot 10^{-11}$ mbar and even more inside the shielding around the STM stage.

Besides the STM, the chamber incorporate six-slot carousel sample storage and tip flashing station that clean the tip from impurities. The transfer between the flashing station, carousel and manipulator is realized with a dual shaft wobblestick manipulator.

Cryostat The design of the Omicron cryogenic system is schematically presented in Fig.1.5. The STM stage is cooled by a liquid bath cryostat system. It comprises two cylindrical tanks, that can be filled separately. The inner tank has a volume of 3l and has the STM stage attached to it. It can be filled either with liquid nitrogen (base temperature $T_{\text{LN}} = 77\text{ K}$) or liquid helium (base temperature $T_{\text{LHe}} = 4.3\text{ K}$). The outer one, with a volume of 3.5 l, is usually filled with liquid nitrogen. Because the LN has one order of magnitude bigger heat of evaporation and is much cheaper than LHe, the outer tank functions as a radiation shield for the inner one in order to reduce its helium consumption. Both tanks are connected to the upper flange of the chamber by three

stainless steel inlet/outlet tubes, used for filling and measuring the level of liquid in the cryostat tanks as well as for letting out the evaporated cooling agent.

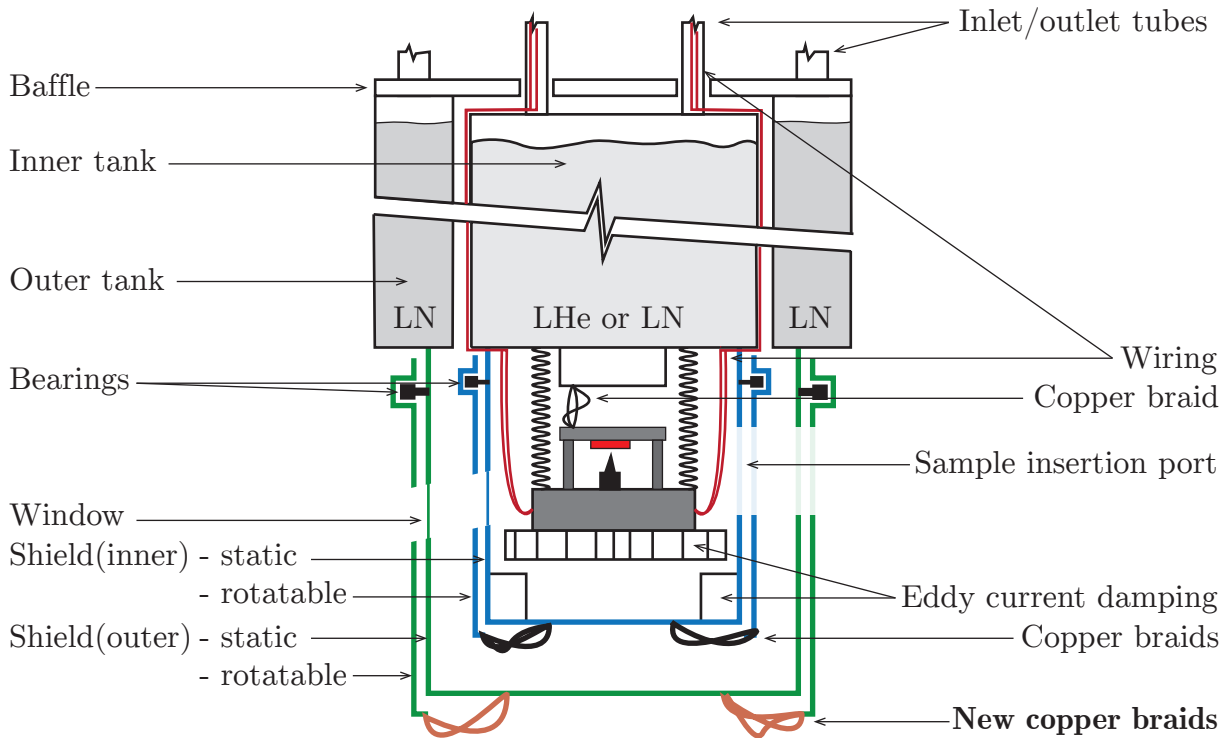


Figure 1.5: Schematic drawing of the cryostat, the radiation shields, the STM stage of the Omicron LT-STM. Indicated addition of the new copper braids between the static and rotational part of the outer shield (shown in brown color) was a part of the system technical modification, that is described in section 1.4.

Since the STM stage has to be optically and mechanically accessible, it can not be completely surrounded by the cryostat tanks. Therefore it is encircled by two cylindrical radiation shields, made of oxygen-free high thermal conductivity copper. Each shield consists of one static cylinder, that is tightly mounted to the corresponding cryostat tank and one rotatable cylinder, that rests on small bearings fixed around the static cylinder. Both shields have four windows for optical access with low heat-radiation transmission rate and one port for sample insertion. By rotating the rotatable cylinders with respect to the static cylinders, it is possible to open a close the access windows and the insertion port to the STM.

STM The STM stage can be either clamped tightly to the inner cryostat tank or it can be released and hang loose on three springs in order to further damp the mechanical vibrations from the outside. A magnetic eddy current damping system is used to damp the oscillations. When released, the thermal contact to the inner tank is carried out by the copper braid. Besides the STM scanning device, the stage is equipped with silicon diode temperature sensor, pyrolytic boron nitride (PBN) heater and superconducting magnet coil (vertical fields up to 3 T).

All the wiring for the STM stage is guided firstly on the outer surface of the inner tank and then along the inlet/outlet tubes. Thus the wires are pre-cooled by the vapours of the cooling agent that rise through the outlet tube. Outside the chamber, the tunneling current is pre-amplified by Omicron SPM PRE 4E amplifier and processed by Omicron

1. EXPERIMENTAL LT-STM SET-UP AND ITS MODIFICATIONS

Matrix control unit. For all measurements presented in this thesis, tungsten tips, prepared by electrochemical etching in NaOH solution, were used.

1.4. Refurbishment of the experimental set-up

The first generation of the Omicron LT-STM, that was described in the previous section, have possessed some technical drawbacks. This section presents all the modifications that have been carried out on the system during the course of this work to improve its performance.

1.4.1. Drawbacks of the original design

The major drawback of the first generation Omicron LT-STM was a short standing time of the cryostat – about 19 hours for the outer tank when filled with LN and about 18 hours for the inner tank when filled with LHe. Therefore, it was necessary to refill both tanks every day and consequently the measurement conditions could not be stable for a longer period. Furthermore, a high helium consumption also affects the price of the measurement time.

The short standing time of the cryostat was mainly caused by the small volume of the tanks, but was also greatly affected by a relatively big thermal bridging of the STM stage to the outer environment through the wires that connected the STM stage and the electrical feedthroughs on the chamber. Moreover, this thermal bridging is a reason for a relatively high base temperature of the system – when the cryostat is filled with LHe, its base temperature is above 5 K, although the temperature of the LHe in the tank is almost one degree less.

Lastly, it was difficult to reach the energy resolution, that was required to perform the scanning tunneling spectroscopy (STS). The difficulties were caused mainly by the original Omicron SPM PRE 4E pre-amplifier. Due to its complexity and the difficulties to access the relevant technical information, the amplifier is inaccessible for user-friendly control of the amplification process and therefore inconvenient for eventual elimination of potential troubles.

1.4.2. Modifications

To address these drawbacks, several improvements have been carried out on the system during the course of this work. It included the upgrade of the radiation protection, the reduction of a thermal bridging by rewiring of the STM stage and a complete change of the electronic control unit and current amplification.

Shielding improvement

As mentioned, the shields protect the STM stage from a thermal radiation from the outside environment. Therefore, it is desirable to keep them at the lowest possible temperature - ideally at the temperature of the tanks with the cooling agent, to which the shields are attached. A proper thermal conductance between the tanks and shields is strongly dependent partly on the shielding material and partly on a proper and tight mechanical contact [37, 38]. For this reason and because the thermal contact through the bearings is inadequate, the rotatable part of the inner shield has a copper braid connection to the static part as indicated in Fig.1.5.

The lack of such copper braid bridging between the static and the rotatable parts on the outer shield can cause higher thermal radiation emitted towards the inner shield through the access ports and therefore increase the cooling agent consumption. To improve this problem, we have installed six new copper braids between the static and the rotatable parts of the outer shield, similarly as on the inner shield (indicated in Fig.1.5). Since the copper braids exert an additional torque on the rotatable part, we also had to add a phosphor-bronze springs to create more friction and prevent spontaneous opening of the shields.

Wiring improvement

According to the Wiedemann-Franz law [38]:

$$\lambda \approx \frac{L_N T}{\varrho}, \quad (1.8)$$

where $L_N = 2.44 \cdot 10^{-8} \text{ W}\Omega\text{K}^{-2}$ is the Lorentz number and T is the temperature, the electrical conductivity ϱ and the thermal conductivity λ are inversely related to each other. When designing a wiring of a cryogenic system, an optimal choice of the material and the diameter of the wire is essential to balance the desired electrical conductivity on one hand and low thermal conductivity on the other.

The original Omicron wiring comprised either copper or phosphor bronze wires. The electrical and thermal properties of these materials are shown in Tab.1.1. Since phosphor bronze has at least one order of magnitude lower thermal conductivity, it is more convenient for cryogenics purposes, unless lower resistivity wires for higher currents are required. In the case of the Omicron systems, copper wires are used only for superconducting magnet coil and the PBN heater. Because the system is a commercial product for a wide field of research, it is prepared for the addition of various optional modules or other kinds of electrical measurements besides STM. For this reason, the original wiring contains a number of spare wires, that are not used. However, these additional wires lead to the thermal bridging of the STM stage with room temperature.

Table 1.1: Composition, electrical resistivity (ϱ) and thermal conductivity (λ) of materials used in the Omicron wiring. [39][40]

Material	Composition	ϱ (293 K) [$\mu\Omega\cdot\text{cm}$]	λ [$\text{W}\cdot\text{m}^{-1}\cdot\text{K}^{-1}$]		
			300 K	80 K	4 K
Copper	100 % Cu	1.7	400	600	300
Phosphor bronze	94.5 % Cu; 5 % Sn; 0.2 % P	11	48	25	1.6
Stainless steel	Fe; Cr; Ni	74	15	7	0.2

The change of the wiring done on the system is summarized in Tab. 1.2. Ten spare wires, that did not guide any signal, were completely removed from the system as well as the two thick copper wires for the superconducting magnet coil, that was not intended to be used. Moreover, two copper wires for the PBN heater were replaced by phosphor bronze wires and the wires to the Si diode were reduced from four to two. This reduction affects slightly the temperature reading because the Si diode can now measure only in two point probe mode instead of four point probe, but the loss of accuracy is not significant for the measurement.

1. EXPERIMENTAL LT-STM SET-UP AND ITS MODIFICATIONS

Table 1.2: Summary of the wiring changes. PhBr – phosphor bronze, Cu – copper, Coax – stainless-steel coaxial cable.

Function	Original		→	New	
	Quantity	Material		Quantity	Material
Si diode	4	PhBr	→	2	PhBr
Grounding of the stage	1	PhBr	→	1	PhBr
Sample pin contacts	4	PhBr	→	4	PhBr
PBN heater	2	Cu	→	2	PhBr
Tunneling current and bias voltage	1	Coax	→	2	Coax
Sample ground	2	Phbr	→	0	–
Spare wires	8	PhBr	→	–	–
Spare wires	4	Cu	→	–	–
SC magnet	2	Cu	→	–	–
Total	35	–	→	20	–

In the original Omicron wiring layout, the bias voltage was applied via capacity coupling on the same coaxial wire, which guides the tunneling current. The sample itself was grounded through a sample-ground phosphor bronze wire. A simplified schematic drawing of the wiring layout is shown in Fig. 1.6a.

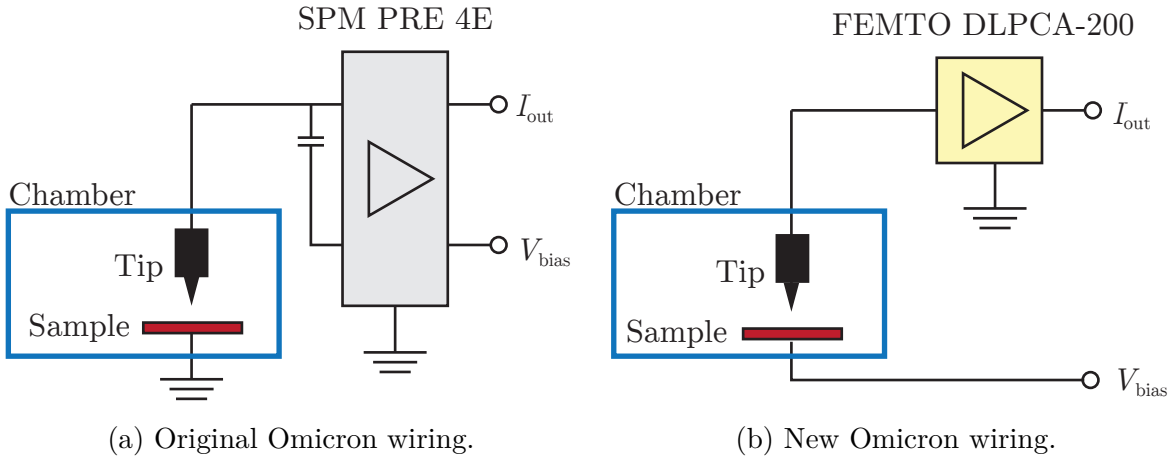


Figure 1.6: Simplified diagram of wiring of the tunneling current I_{out} and the bias voltage V_{bias} before and after the refurbishment. In the original wiring, the bias voltage is coupled to the tunneling current wire through the capacitor. In the new wiring is the bias voltage guided separately directly to the sample.

Because the change of the electronic control unit and the current amplification (described in the subsection 1.4.2) required different wiring layouts, we replaced the tunneling-current and the sample-ground wires by new coaxial stainless steel wires – shown in Fig. 1.6b. The new tunneling-current coaxial wire is connected to the tip as was the former coaxial wire and the bias-voltage coaxial wire is connected to the sample plate instead of the former phosphor bronze wire, that grounded the sample.

To eliminate the noise that can be coupled to the bias voltage cables outside of the chamber between the control unit and the electrical feedthrough flange a low pass filter has been added outside the chamber, just before the feedthrough flange.

Electronics and control unit change

Besides the changes done on the vacuum part of the system, a complete change of the STM control unit and tunneling signal amplification was made outside the LT-STM chamber. The original Omicron SPM PRE 4E preamplifier was replaced by the more simple and user-friendly Variable Gain Low Noise Current Amplifier DLPCA-200 from FEMTO GmbH [41], which, in addition, has a better technical parameters. The Omicron Matrix control unit was changed to the Nanonis Control System made by Nanonis GmbH [42]. Its advantage over the commercial Omicron system is its higher user-friendliness and variability for scanning probe microscopy (SPM) methods.

In combination, the FEMTO amplifier and the Nanonis SPM Control system unit now enable better user control of the signal amplification, signal processing, feedback loop adjustment and device operation.

1.5. Results of the refurbishment and test measurements

After the reassembly, several tests and calibration measurements were carried out in order to evaluate the improvement and to test the system's performance. This included a measurement of the change in the cryostat's standing time and also test measurements of surface topography (STM) and spectroscopy (STS) with the new control unit.

1.5.1. Cryostat standing time change

To test the standing time of the cryostat, both cryostats were first filled with LN, in order to precool them to 77 K. After that the LN in the inner cryostat was replaced by LHe to cool the inner cryostat further down. This is a usual procedure for cryostat cooling to save LHe, which is more expensive and due to its low heat capacity also less efficient for this purpose. When the the base temperature of 4.4 K was reached, both cryostats were refilled again and the time measurement began.

It was expected that, due to the radiation shielding improvement and the elimination of unnecessary thermal bridging, the standing time of the inner cryostat will significantly improve. And indeed, the standing time of the inner cryostat, when filled with the liquid helium (LHe), increased by a factor of 2, from 19 hours before the refurbishment to 40 hours after it. Furthermore, the base temperature of the STM stage T_{base} , measured by the Si diode, decreased from 4.9 K to 4.4 K.

1.5.2. STM and STS test measurements

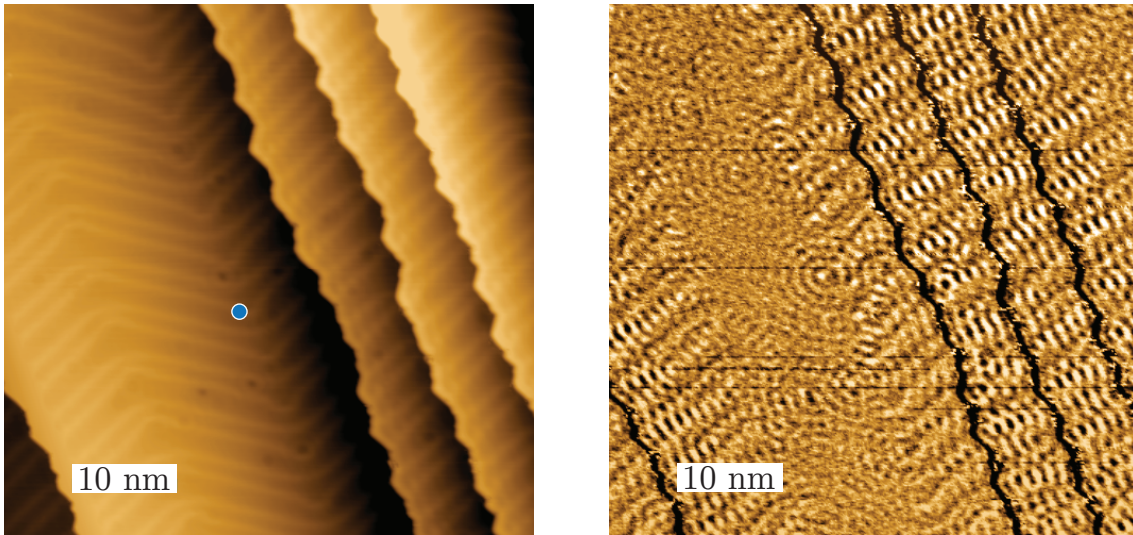
In order to test the performance of the system with the new electronics and control unit, two samples were investigated. First, we acquired the topography images, dI/dV maps and differential conductance spectra of the Au(111) surface to test the general functionality of the system techniques. Secondly, a superconducting gap (SC) in differential conductance spectra on a Pb(111) crystal was measured to test the energy resolution for the system. By fitting the measured differential conductance data of the SC gap, an effective electron temperature could be determined.

1. EXPERIMENTAL LT-STM SET-UP AND ITS MODIFICATIONS

Au(111)

Because of the famous and well studied $22 \times \sqrt{3}$ herringbone reconstruction [43] and easy surface preparation, Au(111) crystals are often used for STM calibration measurements. It has also been known, that the Au(111) surface has a surface localized Shockley state [44] with a band edge 0.52 eV below the Fermi energy (E_F) [45]. This state originates from different boundary conditions for electron wave functions at the surface-vacuum interface and is localized only in a few surface atomic layers. Defects such as adsorbates, vacancies and step edges can act as scattering centres for the electrons, creating a standing wave pattern around them [46].

After several cleaning cycles of Ar^+ ion dynamic sputtering and annealing at 500 °C for 10 min, the Au (111) sample was inserted into the STM stage, that was cooled down to LN temperature. Fig. 1.7a shows a topography image of the clean Au(111) surface with the several step edges and apparent herringbone reconstruction. Fig. 1.7b shows a simultaneously measured spectroscopy image that reveals a clear scattering wave pattern. The image shows interference of two types of the scattering pattern – a parallel standing waves pattern near the step edges and a radial standing wave pattern around the point defects on the flat surface.



(a) Topography image.

(b) Spectroscopy image.

Figure 1.7: (a) The image of the clean Au (111) surface with several atomic steps and visible herringbone reconstruction. The blue dot marks the position of the dI/dV spectrum presented in Fig.1.7. (b) The simultaneously measured spectroscopy image with visible standing wave pattern. ($V_{\text{bias}} = 200$ mV, $I_{\text{setp}} = 800$ pA)

Subsequently a differential conductance spectrum was taken on the Au(111) terrace in the energy range between -0.8 V and 0.4 V (shown with blue line in Fig. 1.7; the position on the surface indicated by a blue dot in Fig. 1.7a). At approximately -0.5 V below Fermi energy E_F we can see the band edge of the Shockley surface state.

Attempts to obtain a differential conductance spectrum on Au(111) were done on this Omicron system also before its refurbishment, but due to the problems with signal amplification and noise no data with distinguishable features were obtained, even after a several weeks lasting effort. Representative data of differential conductance measurements with the old Omicron electronics are shown with the red line in Fig. 1.7. The

data are displayed only for schematic comparison of the system performance before and after the refurbishment. No qualitative comparison could be made because of completely different measurement and technical parameters. However, we can see that after the refurbishment, we were able to measure spectra with apparently more pronounced surface state features with significantly lower effort.

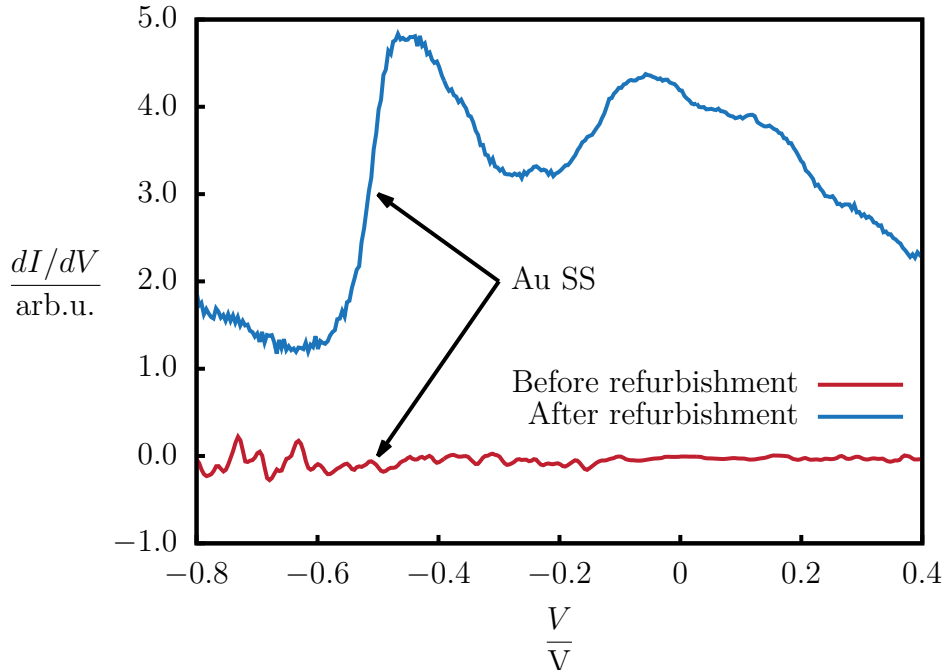


Figure 1.8: The differential conductance of the Au(111) surface on the position indicated in Fig.1.7a for an energy range between -0.8 V and 0.4 V (blue line). Spectra on the Au(111) surface for the same energy range obtained with the old Omicron electronics for schematic comparison (red line). The spectra are not renormalized or offset, but can not be qualitatively compared because of completely different technical a measurement parameters.

All in all, functionality of the STM set-up after the replacement of the electronics, the signal amplifier and the main control unit of the Omicron system, proved to be successful as is indicated by the presented data. System now posses more variability and direct user control over the STM and STS measurements.

Pb(111)

To test the energy resolution of the STS, the Pb(111) crystal was investigated by measuring a differential conductance spectrum in a small energy range around E_F aiming to observe its superconducting gap.

Bulk lead is a type-I superconductor with the third highest critical temperature among the pure element superconductors ($T_C = 7.19\text{ K}$) [28][31]. It has a superconducting energy gap $\Delta = 1.1\text{ meV}$ [47]. Therefore the quasiparticle peaks should be visible on the differential conductance spectra at $\pm 2\Delta = \pm 2.2\text{ meV}$ [48].

Because the Pb(111) crystal was stored for a long time in ambient conditions outside the UHV chamber, a blueish oxide layer was formed on its surface. In order to prepare a suitable surface for measurement, it had to be cleaned by many cycles of Ar^+ sputtering, followed by annealing at $200\text{ }^\circ\text{C}$ for 2 hours in the preparation chamber before transferring

1. EXPERIMENTAL LT-STM SET-UP AND ITS MODIFICATIONS

it to the STM stage. To observe a superconductivity phenomena, temperature below characteristic T_C has to be reached. By performing measurements at low temperature we also increase the measurement stability and lead to a lower thermal broadening of electronic features. For these reasons, all the STM/STS measurements were carried out at LHe temperature.

In Fig. 1.9, a representative differential conductance spectrum in the energy range between -10 mV and 10 mV is presented. It is an averaged spectrum of fifty bias sweeps over one point above the surface. Measured data points are represented by red crosses and the blue line shows a theoretical data fit produced by a MATLAB script. We find, that the measured data show the expected energy gap and quasiparticle peaks at energy around ± 2.2 meV.

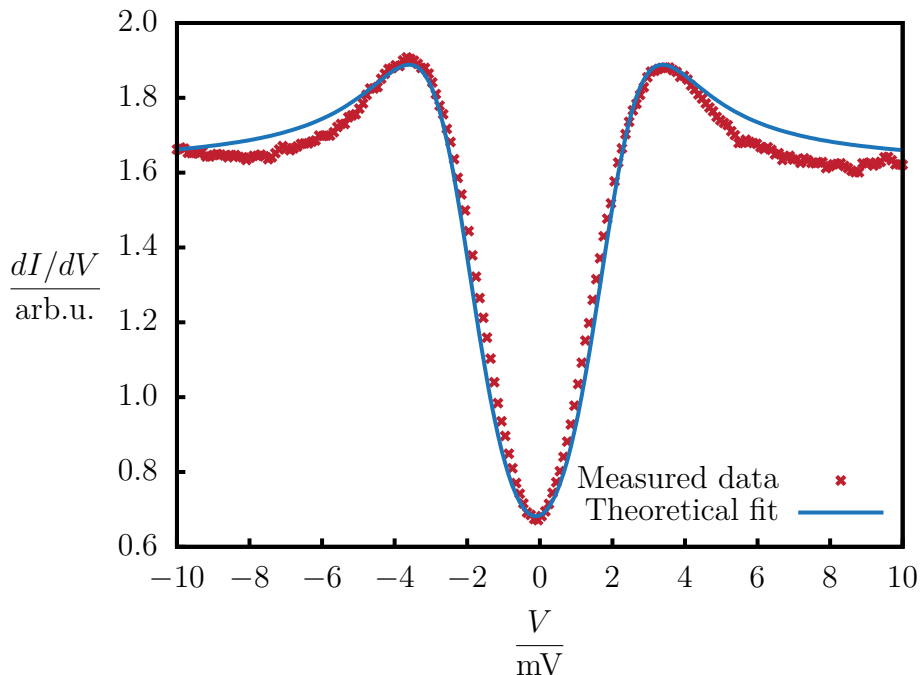


Figure 1.9: The differential conductance data (red crosses) measured on the Pb(111) crystal averaged over 50 sweeps and a theoretical fit (blue line) with following parameters: $T_{\text{ef}} = 4.8$ K, $\Gamma = 0.84$ mV, $\Delta = 1.1$ meV, $V_{\text{mod}} = 0.2$ mV. Visible superconducting energy gap with quasiparticle peaks at energy around ± 2.2 meV.

The MATLAB script, developed in the SPM group in Hamburg and modified during the work on this thesis, calculates the theoretical curve by a convolution of the density of states with the Fermi-Dirac distribution for following optional parameters: effective electron temperature (T_{ef} [K]), energy gap (Δ [mV]), quasiparticle lifetime broadening (Γ [mV]) and modulation voltage of the lock-in amplifier (V_{mod} [mV]). Because the SC energy gap of lead Δ and modulation voltage V_{mod} are known, only T_{ef} and Γ were changed during the data fitting. The fitting was done by a combination of parameter adjustment with immediate eye control and subsequent minimization of a root mean square value between measured data and suggested theoretical curve.

The theoretical curve in Fig.1.9 is fitted with parameters $T_{\text{ef}} = 4.8$ K and $\Gamma = 0.84$ mV. Since the fitting is significantly influenced by a human factor and no proper fitting statistics could be done, a type B uncertainty is the most important for the accuracy of the

1.5. RESULTS OF THE REFURBISHMENT AND TEST MEASUREMENTS

result. In this case, it was estimated to be about ± 0.3 K. Because of this, the effective electron temperature of the sample was evaluated to $T_{\text{ef}} = (4.8 \pm 0.3)$ K.

This result confirmed the achievement of the desired energy resolution for STS on the Omicron system after the refurbishment and determined an effective electron temperature of the samples on the STM stage.

1. EXPERIMENTAL LT-STM SET-UP AND ITS MODIFICATIONS

2. Preparation of superconducting-magnetic interfaces

A lot of studies investigating the magnetism on the nanoscale have already been published [1–4]. Furthermore, researchers explored the possibilities of preserving the superconductivity in superconducting materials when reaching the ultrathin film limit [6, 49]. By combining these two phenomena, a relatively new and interesting field might be opened up in surface science [7].

My work was a part of a bigger research project whose ultimate goal is to study the interplay between magnetism and superconductivity on the atomic scale by means of LT-STM. The desired final state of the superconducting-magnetic interface is depicted in Fig. 2.1. This part of my work aimed mainly on the first step towards this goal – the preparation of a stable superconducting-magnetic interface. This included the following:

1. Finding a suitable substrate and materials for magnetic and superconducting films.
2. Preparing an atomically flat and clean substrate surface.
3. Controlling the individual growth of both magnetic and superconducting films on the desired substrate while preserving their magnetic, respectively superconducting, properties.
4. Controlling the growth of the films on top of each other.



Figure 2.1: Schematic drawing of the desired superconducting-magnetic interface preparation. The magnetic film is first deposited onto the clean and atomically flat substrate. Subsequently a superconducting film is deposited partially over the magnetic film.

2.1. Choice of the material

This section presents the main reasons for the material choice and specifies the major goal of this project (beyond the scope of this work).

2.1.1. Substrate and magnetic film

W(110) and Ir(111) were chosen as suitable substrates for two general reasons. First, they have both been well studied in the past and their cleaning procedure is known and tested. Second, epitaxially grown islands of iron or manganese monolayers on both substrates show interesting magnetic properties, that we wanted to utilize as a magnetic component of the desired superconducting-magnetic interface. This fact also determined the choice of iron as the material for the magnetic film component.

Majorana fermions observation

By bringing a conventional superconductor into the proximity of a topologically non-trivial system in the presence of a magnetic field, a different state of matter, a topological superconductor, can be created. At the edge of such topological superconductor, Majorana fermions are predicted to confine [7, 50]. The high spin orbit interaction of iridium and tungsten make them a good candidates to host topological phases.

Ir(111) is used as a substrate for various 2D structures, for example as a substrate for graphene layers [51]. But the important reason for choosing an Ir(111) substrate for this project is the fact that Heinze *et al.* showed a formation of spontaneous magnetic nanoskyrmion lattice on monolayer iron films on Ir(111) surface [3]. They presented a pattern of a non-collinear spin texture as a magnetic ground state of a hexagonal Fe film.

Similar to Fe/Ir(111) magnetic behaviour, Bode *et al.* [52] published a study of monolayer manganese films on W(110), that exhibited a spontaneous magnetic nanoskyrmion lattice. Moreover, lot of different aspects of magnetism has been studied on W(110) by spin polarized STM, e.g. observation of superparamagnetic iron islands [1].

Mentioned magnetic nanoskyrmion lattices could serve as the topologically non-trivial magnetic systems for creating the desired nanoscale superconducting-magnetic interface. This can lead to the creation of a topological superconductor state of matter and open the possibility for observation of Majorana fermions.

2.1.2. Superconducting film

For the choice of the superconducting material, it was important to find a material that would grow in continuous, atomically flat films on top of the substrate and magnetic film without a big lattice mismatch, strain or alloying. For this, we had several options in our experimental set-up: Vanadium (Bulk $T_C = 5.4\text{ K}$), Niobium (Bulk $T_C = 9.2\text{ K}$), Tantalum (Bulk $T_C = 4.5\text{ K}$), Aluminum (Bulk $T_C = 1.2\text{ K}$), Lead (Bulk $T_C = 7.2\text{ K}$). It has to be noted that all the mentioned T_C values apply for bulk crystals and in the thin film limit they strongly depend on the size, thickness and structure of the film [5, 6]. Since the growth and characterization of thin films of these superconducting materials on W(110) and Ir(111) had not been investigated yet, the characterization of the growth was of primary importance in the course of this work.

After mastering the substrate cleaning process (section 2.2), we planned to first reproduce the formation of magnetic iron films (section 2.3) and then investigate the growth of thin superconducting layers, starting with the growth of vanadium (section 2.4 and 2.5)

2.2. Substrate preparation

This section describes the cleaning procedure of both W(110) and Ir(111) substrates. Although the cleaning procedure is well known for both substrates [10, 51], they were prepared for the first time in this experimental set-up and the procedure had to be adapted for our system.

2.2.1. W(110) preparation

Tungsten is a transition metal from the sixth period of the periodic table with the $5d^4$ configuration. It has the highest melting point of all the elements $T_m = 3422\text{ °C}$ [53] in the periodic table. Fig. 2.2a shows a tungsten bcc crystal structure (lattice constant $a_W = 3.16\text{ Å}$) with indicated W(110) plane crystalline orientation, that was used in the course of this work. The W(110) crystal plane is depicted in Fig. 2.2b (red circles).

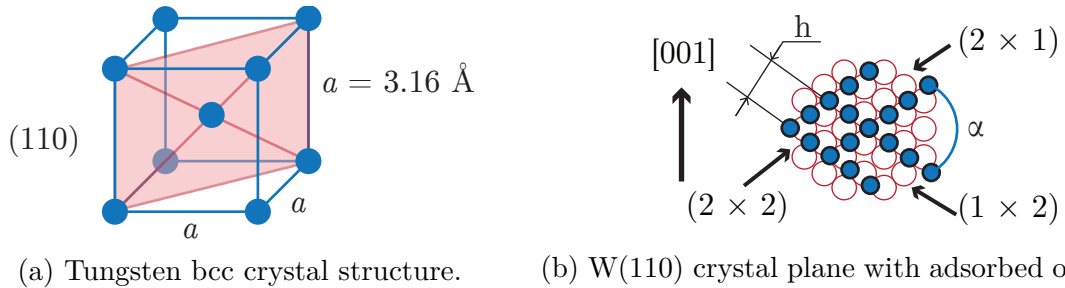


Figure 2.2: (a) Tungsten bcc crystal structure with the lattice constant $a_W = 3.16\text{ Å}$ and indicated W(110) plane. (b) The theoretical arrangement of adsorbed oxygen (blue dots) on the W(110) plane (red circles) according to Johnson *et al.* [54]. The span between the oxygen rows h and the angle α can be calculated from the W(110) plane geometry as $h = 5.16\text{ Å}$ and $\alpha_O = 109.5^\circ$.

The preparation procedure for an atomically flat W(110) surface has been reported elsewhere [8–10]. Its aim is to remove the main impurity present in the tungsten crystal – carbon atoms.

The procedure consists of 2-step cycles, that are repeated several times in a row. It starts with sample annealing under a partial oxygen pressure, followed by a rapid temperature flashing at UHV conditions. The temperature and ambient pressure values for both steps are for comprehensibility presented in the Tab. 2.1. During the first step of the cycle, carbon diffuses out from the bulk crystal to the surface, where it reacts with the ambient oxygen, forming CO and CO₂. The majority of these substances then desorbs from the surface and can be pumped out of the chamber. The residual CO and CO₂ molecules as well as the adsorbed oxygen, that stick to the surface during the annealing, can be thermally desorbed in the second step of the cleaning cycle by a rapid temperature flashing above $T_f = 2000\text{ °C}$.

Table 2.1: Summary of the values for both steps of the W(110) cleaning procedure.

	Time	Temperature [°C]	Pressure [mbar]
1st step	30 min	$T_a \sim 1300$	Oxygen in the range ($2 \cdot 10^{-8}$, $5 \cdot 10^{-7}$)
2nd step	10 s	$T_f > 2000$	UHV $< 2 \cdot 10^{-9}$

2. PREPARATION OF SUPERCONDUCTING-MAGNETIC INTERFACES

The W(110) sample was mounted on the tungsten sample plate, that was heated by an electron bombardment heater in the preparation chamber. The temperature was measured with a pyrometer. We decided to read the temperature from the sample plate near the mounted sample. This way we could calibrate the temperature reading for a case of mounting different samples in the future. On the other hand, this fact can cause problems with measuring the exact temperature of the sample, because it can differ from the temperature of the sample plate due to the bad thermal contact between them.

The first preparation consisted of seven cycles, during which we gradually decreased the oxygen pressure in each cycle from $P_{O_2} = 5 \cdot 10^{-7}$ mbar to $P_{O_2} = 2 \cdot 10^{-8}$ mbar. The annealing temperature, read by the pyrometer, was kept constant at $T_a = 1300$ °C in each cycle as well as the flashing temperature $T_f = 2000$ °C. Fig. 2.3a shows the state of the surface after the first preparation. It can be seen that the tungsten is forming a flat steps that are distinguishable across the image. The features on the image are not ideally sharp, due to the unstable and blunt tip. Despite the poor image quality, the apparent surface contamination demonstrated the necessity to repeat the cleaning process.

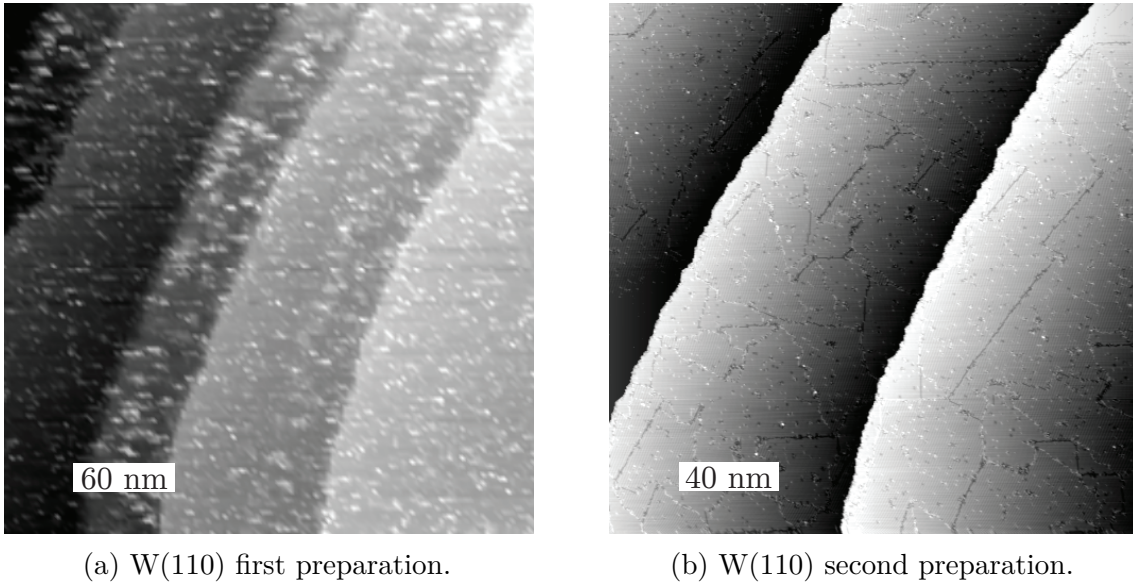


Figure 2.3: (a) Representative image of a dirty W(110) surface with several atomic steps after the first cleaning procedure. The quality of the image is not perfect, but sufficient for determining the state of the cleaning process. (b) Representative image of W(110) surface after the second preparation without apparent adsorbates, but visible stripy features. The height of the steps is $h = (2.1 \pm 0.1)$ Å. (Both $V_{\text{bias}} = 500$ mV, $I_{\text{setp}} = 500$ pA)

Oxygen reconstruction

The second preparation followed the same pattern as the previous one, resulting in an improved state of the surface. In Fig. 2.3b we can see more than 100 nm wide terraces with a height of $(h = 2.1 \pm 0.1)$ Å. This is comparable with the calculated theoretical value of $h = \sqrt{2} \cdot a_W / 2 = 2.23$ Å. Although the surface was visibly more clean than in Fig. 2.3a a closer inspection revealed a stripy pattern on the terraces (Fig. 2.4a and Fig. 2.4b).

Johnson et al. [54] presented a STM study of an oxygen adsorption on the W(110) surface in three ordered reconstruction phases: (2×1) , (2×2) and (1×1) . The first two are

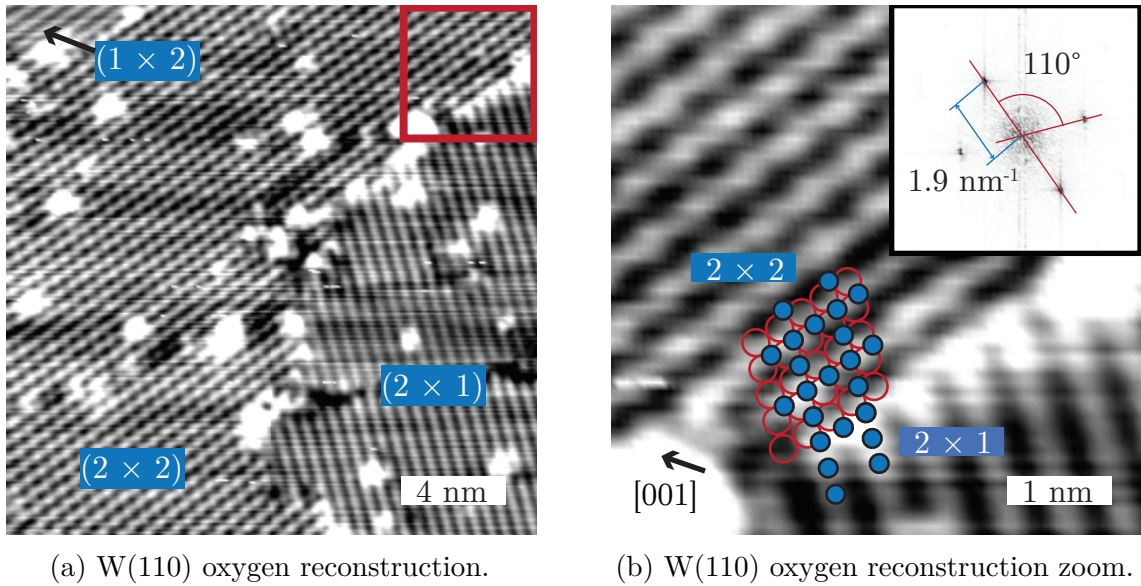


Figure 2.4: (a) Representative image of an oxygen reconstruction on the W(110) surface with marked areas of (2×1) , (1×2) and (2×2) reconstruction. The red square marks the zoom shown in (b). (b) Zoom on the previous image with fitted theoretical reconstruction of adsorbed oxygen. The inset shows the 2D-FFT of the image with the measured reciprocal distance between the rows and angle between the rows of complementary phases (2×1) and (1×2) . (Both $V_{\text{bias}} = 100 \text{ mV}$, $I_{\text{setp}} = 1 \text{ nA}$)

depicted in Fig. 2.2b. It shows adsorption of oxygen along the $\langle 111 \rangle$ directions. The distance between the rows of oxygen in the (2×1) phase can be calculated from the W(110) plane geometry as $h = 5.16 \text{ \AA}$. There exists also a (1×2) phase along complementary $\langle 111 \rangle$ direction with the same row span. The angle between these directions can be calculated as $\alpha_{\text{O}} = 109.5^\circ$.

By further analysis of the 2D Fourier transformation ($k = 1/\lambda$ convention, shown in inset of 2.4b) of the STM images 2.4a and 2.4b, we could determine the distance between the rows in the real space as $h = (5.26 \pm 0.23) \text{ \AA}$ and angle as $(\alpha_{\text{O}} = 110 \pm 3)^\circ$. These values are in very good agreement to the published and calculated values presented in the previous paragraph for the oxygen absorption. A good fit of the theoretical phase reconstruction could be then made as presented in Fig. 2.4b. From this we could conclude, that the surface was partially covered with adsorbed oxygen.

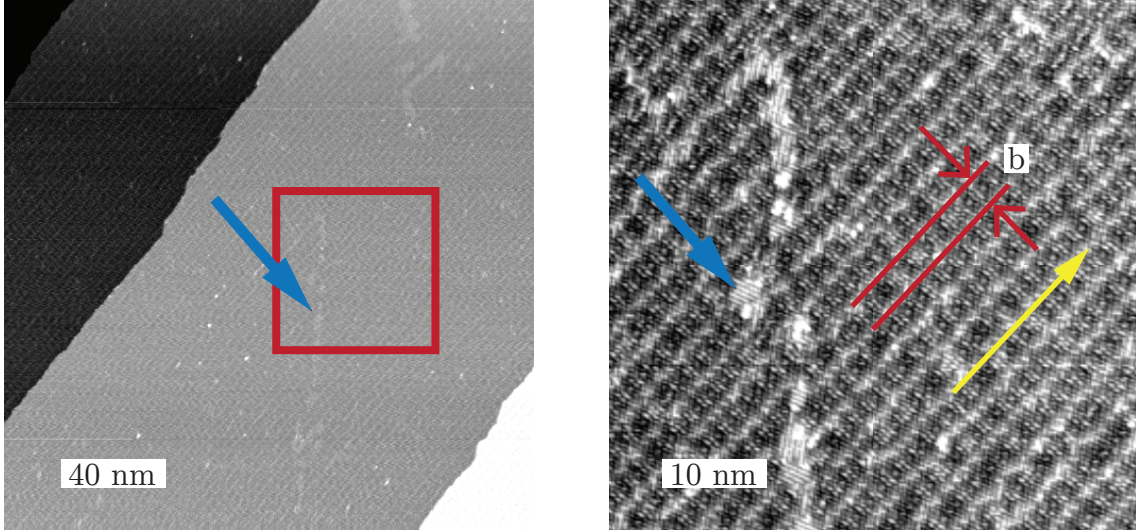
Because the oxygen is supposed to thermally desorb during the rapid temperature flashing of the sample above 2000°C , we deduced that the annealing temperature is not high enough. This was caused probably by the inaccurate calibration of the pyrometer and also because the temperature was not measured directly on the sample, but next to it. Thus, we decided to increase the flashing temperature, measured by the pyrometer, by 150°C for the next cleaning procedure.

Carbon reconstruction

The increase in the flashing temperature to $T_f = 2150^\circ\text{C}$ in the second step of the cleaning procedure proved to be sufficient to remove the majority of the adsorbed oxygen from the surface. Representative images of the surface after the modified cleaning procedure are displayed in Fig. 2.5a and Fig. 2.5b. The height of the step is $h = (2.2 \pm 0.3) \text{ \AA}$. The blue arrows in both images point onto areas of residual adsorbed oxygen, where a stripy

2. PREPARATION OF SUPERCONDUCTING-MAGNETIC INTERFACES

pattern similar to 2.4a can be seen. The rest of the surface shows apparently a different pattern. The measured perpendicular distance between these rows is $b = (31.1 \pm 2.3) \text{ \AA}$.



(a) W(110) carbon reconstruction.

(b) W(110) carbon reconstruction zoom.

Figure 2.5: Images of assumed carbon reconstruction on the W(110) surface. Blue arrows mark the position of areas with residual adsorbed oxygen. The distance between the characteristic rows of carbon reconstruction $b = (31.1 \pm 2.3) \text{ \AA}$ is comparable wto the literature value $b_{\text{lit}} = 31.7 \pm 3 \text{ \AA}$. The distance between the periodic structures along the direction indicated by the yellow arrow differs ($\sim 20\%$) from the literature values. (Both $V_{\text{bias}} = 1 \text{ V}$, $I_{\text{setp}} = 500 \text{ pA}$)

The distance between the rows can be compared with the distance of the carbon $R(15 \times 12)$ reconstruction reported in literature [8, 55]. Accordingly, the perpendicular distance between the rows on the carbon reconstructed surface is $b_{\text{lit}} = 31.7 \pm 3 \text{ \AA}$ [8], which is consistent with the values measured by us. On the other hand, the periodicity of the structure in the direction parallel to the rows (indicated by the yellow arrow) differs significantly ($\sim 20\%$) form the observed value. Since it was not the main goal of this project to study carbon on W(110), we did not investigated the structure in more detail, but it could possibly represent some new carbon reconstruction. Nevertheless, this meant that the surface is probably still saturated with carbon and further cleaning cycles are necessary to acquire a clean W(110) substrate.

At this point of the cleaning process we realized that the intended use of W(110) as a substrate for studying the growth of thin vanadium layers could be problematic, because the vanadium alloys easily with tungsten [56] when heated together. And since the W(110) is standardly cleaned by annealing and rapid temperature flashing up to $2000 \text{ }^\circ\text{C}$, we would risk the alloying of these two substances and the crystal poisoning. Because the development of a safe sputtering W(110) cleaning method was not in the time limit of this work, we decided to focus first on the Ir(111) sample.

2.2.2. Ir(111) preparation

Iridium is a transition metal from the sixth period of the periodic table with the $5d^7$ configuration. In comparison to tungsten, its melting point is almost $1000 \text{ }^\circ\text{C}$ lower ($T_{\text{m}} =$

= 2460 °C) and iridium crystals to the fcc structure (Fig. 2.6a) with a lattice constant $a_{\text{Ir}} = 3.84 \text{ \AA}$ [57]. Fig. 2.6b shows the investigated Ir(111) plane crystalline orientation.

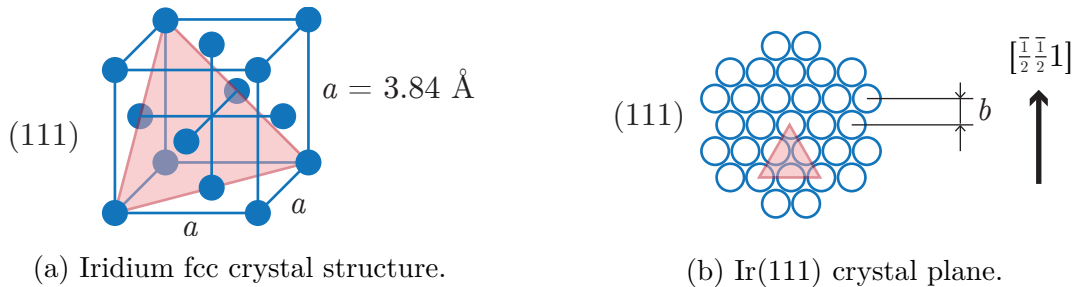


Figure 2.6: (a) Iridium fcc crystal structure with the lattice constant $a_{\text{W}} = 3.84 \text{ \AA}$ and indicated W(110) plane. (b) Ir(111) crystal plane. The red triangle corresponds to the red triangle in (a). The calculated distance between the closest rows of atoms is $b = 2.34 \text{ \AA}$.

Because iridium has a much lower melting point than tungsten and therefore can not be heated to high temperatures, the usual cleaning procedure [51, 58] differs from the tungsten one by replacing the rapid temperature flashing step by Ar^+ ion dynamic sputtering. This means that we would not later risk the alloying with vanadium, because all the surface atoms are removed by the sputtering at the room temperature before annealing.

The Ir(111) sample was mounted on the molybdenum sample plate, that was heated by an electron bombardment heater in the preparation chamber. The temperature was measured the same way as described for tungsten in the previous subsection.

In the first step of the Ir(111) cleaning procedure we used a dynamic sputtering with Ar^+ ions accelerated to an energy of $E_{\text{Ar}} = 1 \text{ keV}$ to remove the topmost surface layers. The second step was the same as for tungsten – carbon from the bulk crystal was extracted by annealing under partial oxygen pressure. The annealing step also provides iridium atoms with sufficient energy to overcome the diffusion barrier and they can migrate on the surface to the most favourable energy position. This leads to re-creation of an atomically flat surface. After several sputter-annealing cycles, the oxygen is still adsorbed on the surface as in the case of the tungsten preparation. To thermally desorb it, the last step of the procedure was the sample temperature flashing at $T_{\text{a}} = 1500 \text{ °C}$. Since the flashing temperature is markedly lower than for the tungsten crystal, the sample had to be flashed for a longer time. The correct sputtering energy, temperature and ambient pressure values for all steps are for comprehensibility presented in the Tab. 2.2.

Table 2.2: Summary of the values all steps of the Ir(111) cleaning procedure.

1st step	15 minutes of Ar^+ sputtering ($E_{\text{Ar}} = 1 \text{ keV}$)		
	Time	Temperature [°C]	Pressure [mbar]
2nd step	15 min	$T_{\text{a}} \sim 1300$	Oxygen $2 \cdot 10^{-7}$
3rd step	2 min	$T_{\text{f}} \sim 1500$	UHV $< 2 \cdot 10^{-9}$

The state of the Ir(111) surface got well after only a few cycles. Fig. 2.7a shows a representative topography image of the Ir(111) surface. There are visible steps of height $h = (2.24 \pm 0.32) \text{ \AA}$, which is in good agreement with calculated theoretical value $h = 2.21 \text{ \AA}$ for atomic terrace of iridium. The average width of the observed iridium terraces was determined as $w = 100 \text{ nm}$. Later in the course of this work, when the cleaning

2. PREPARATION OF SUPERCONDUCTING-MAGNETIC INTERFACES

procedure was well established, we could observe even wider steps with a width of more than 300 nm.

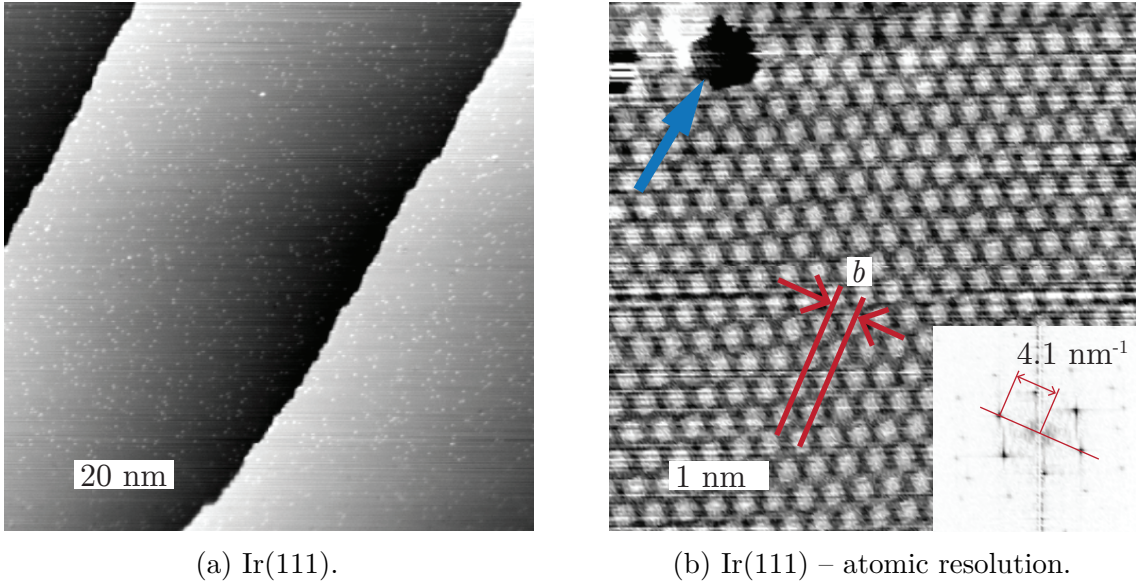


Figure 2.7: (a) Representative image of the cleaned Ir(111) surface with atomic terraces of height $h = (2.24 \pm 0.32) \text{ \AA}$ and average width $w = 100 \text{ nm}$. ($V_{\text{bias}} = 1 \text{ V}$, $I_{\text{setp}} = 500 \text{ pA}$) (b) Image showing an atomic resolution of the surface with missing atoms in the lattice (blue arrow). The inset shows the 2D-FFT of the STM image with measured reciprocal distance between the rows of atoms – the corresponding distance b in real space is represented by red lines in the STM image. ($V_{\text{bias}} = 4 \text{ mV}$, $I_{\text{setp}} = 26 \text{ nA}$)

In Fig.2.7b an atomic resolution image obtained on the cleaned Ir(111) surface is presented. The inset shows the 2D Fourier transformation ($k = 1/\lambda$ convention) of the atomic structure. From the FFT reciprocal space, the average distance between the closest atom rows (marked by the red line) was determined as $b = (2.44 \pm 0.27) \text{ \AA}$. This also agrees with the theoretical calculated value for the Ir(111) plane $b = 2.34 \text{ \AA}$. The blue arrow marks missing atoms in the surface plane, torn off from the surface by the tip during the scanning.

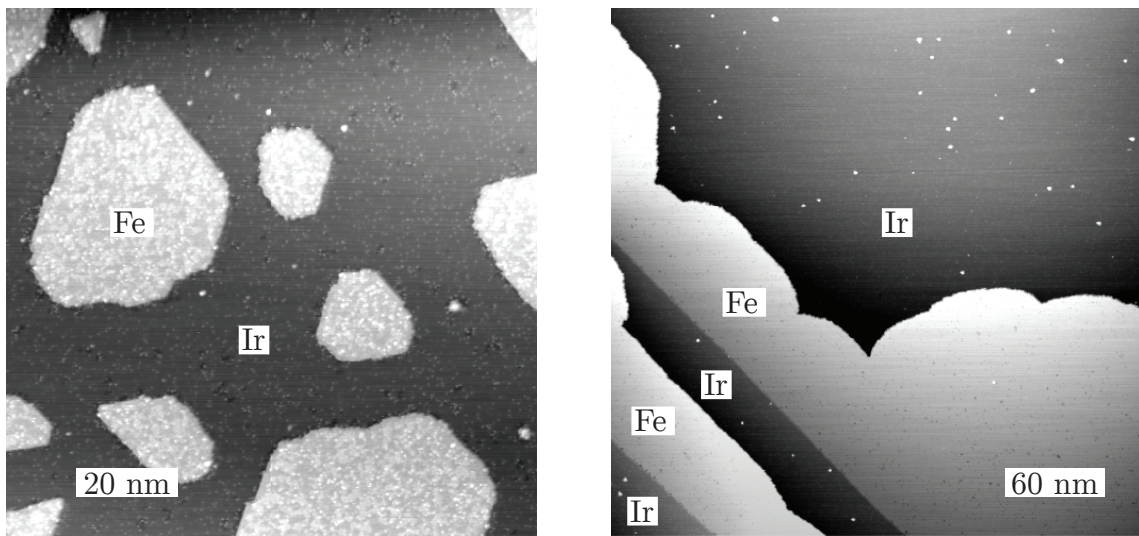
To sum up, we succeeded in developing suitable cleaning procedure for preparing Ir(111) surface with wide atomic terraces. This was confirmed by reaching atomic resolution on the Ir(111) plane with correct dimensions.

2.3. Growth of Fe on Ir(111)

Iron belongs to the group of transition metals and is located in the fourth period of the periodic table. It has a $3d^6$ configuration. Bulk iron crystallizes in bcc structure with a lattice constant of $a = 2.87 \text{ \AA}$ [57]. However, Bergman *et al.* demonstrated its pseudomorphic epitaxial growth on an Ir(111) substrate [59]. The first atomic layer of iron accommodate the fcc lattice structure of the Ir(111) substrate, but the second layer already shows strain-relief structures. Moreover, Bergman *et al.* observed a complex magnetic structure in the first atomic layer with spin polarized STM, when the sample was cooled down to LHe temperature. The structure was later identified by Heinze *et al.* as a formation of a spontaneous magnetic nanoskyrmion lattice [3].

The growth of the iron film and observation of the nanoskyrmion magnetic phenomena has already been reproduced in our group in the past, but in a different experimental set-up. Our goal was to reproduce the growth in our set-up and create an iron film in form of monolayer "wires" along the iridium step edges.

Before each iron deposition, the substrate was cleaned by the iridium cleaning procedure described in section 2.2.2. The iron was deposited using an electron beam evaporator. For the first deposition, we evaporated iron from onto the clean substrate at room temperature. Subsequently the sample was annealed for 11 min at $T_a = 380^\circ\text{C}$. Fig. 2.8a shows the state of the surface after the first deposition and annealing. Surface is homogeneously covered with monolayer iron islands with an average width of 30 nm. From several scans on different areas on the surface, we could conclude there is no obvious preferential surface diffusion towards the iridium step edges. Moreover, there is a visible contamination of unknown origin on the surface of all iron islands.



(a) Iron on Ir(111).

(b) Iron on Ir(111).

Figure 2.8: (a) Representative image of iron islands on the Ir(111) surface after a deposition at room temperature and post annealing to $T_a = 380^\circ\text{C}$. Iron homogeneously covers the substrate without any tendency to diffuse towards the step edges. Iron islands are covered with adsorbates of unknown identity. (b) Representative image of iron on the Ir(111) surface after deposition onto the warm sample ($T_a = 300^\circ\text{C}$) without additional post-annealing. The height of the iron layer is $h_{\text{Fe}} = (2.5 \pm 0.2) \text{ \AA}$ and the height of the iridium step edge is $h_{\text{Ir}} = (2.0 \pm 0.2) \text{ \AA}$. (Both $V_{\text{bias}} = 1 \text{ V}$, $I_{\text{setp}} = 500 \text{ pA}$)

Later we discovered that the contamination of the iron islands was not due to the deposition procedure. As we measured the STM images more than twelve hours after the deposition and the sample was positioned in the STM at 77 K during that period, the contamination was probably caused by the dirt desorbing from the cryostat shield walls. And since iron is more reactive than iridium, the effect is more apparent on the iron islands than on the substrate. The easiest way address this issue is to perform measurements right away after the preparation. For long-period measurements, it would be necessary to measure at LHe temperatures, when the majority of contaminants is sticking to the cryostat.

To achieve the surface diffusion of iron towards the iridium step edges, we decided to slightly change the preparation procedure – for the next deposition we evaporated the iron

2. PREPARATION OF SUPERCONDUCTING-MAGNETIC INTERFACES

on the warm substrate at $T_a = 300^\circ\text{C}$ with no post-annealing. A representative image of the surface is presented in Fig. 2.8b. The measurement was performed soon after the deposition and no major contamination was observed at this time. The majority of the deposited iron has apparently diffused to the iridium step edges, creating monolayer iron "wires" along them, exactly as desired. The height of the iron layer is $h_{\text{Fe}} = (2.5 \pm 0.2) \text{ \AA}$, which is approximately 0.5 \AA higher than the height of iridium step $h_{\text{Ir}} = (2.0 \pm 0.2) \text{ \AA}$ (consistent with the height of clean iridium in Fig. 2.7a).

Fig. 2.9 presents an image obtained on the iron layer with visible atomic resolution. The lattice shows a hexagonal structure with threefold symmetry. By analysis of the reciprocal image in 2D-FFT (shown in the inset, $k = 1/\lambda$ convention), we determined the distance between the closest rows of atoms as $b = (2.39 \pm 0.17) \text{ \AA}$ (marked by the red lines in the STM image), which agrees with the previously observed span of iridium atomic rows on clean Ir(111) surface in subsection 2.2.2. This observation is in agreement with the published pseudomorphic growth of iron on the Ir(111) substrate.

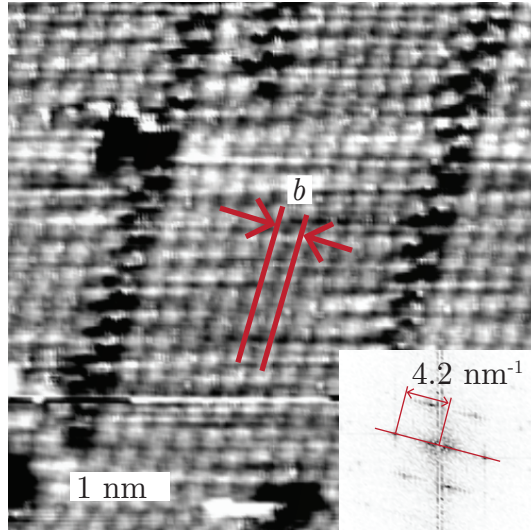


Figure 2.9: Image obtained on the iron monolayer on Ir(111) substrate with apparent hexagonal structure. The inset shows its 2D-FFT from which we determined the span of the atomic rows (marked by red lines in the STM image) as $b = (2.39 \pm 0.17) \text{ \AA}$. ($V_{\text{bias}} = 5 \text{ mV}$, $I_{\text{setp}} = 7.4 \text{ nA}$)

To conclude this part, we successfully created the magnetic component of the desired superconducting-magnetic interface by reproducing the iron growth on Ir(111) substrate in the form of monolayer "wires" along iridium step edges. The pseudomorphic growth of Fe on Ir(111) was confirmed by matching the dimensions of the observed iron lattice to the values measured previously on clean Ir(111). To reproduce the observation of nanoskyrmion lattice would require a magnetic tip and measurements at the LHe temperature. Because the skyrmion lattice formation on the iron-iridium system has already been reproduced in the other experimental set-up in our laboratory, we decided it was not necessary to try reproducing it at this stage of the project. Thus we moved towards the investigation of the superconducting component of the desired interface, namely the study of the vanadium growth on the Ir(111) substrate.

2.4. Growth of V on Ir(111)

Vanadium is, like iron, a transition metal from the fourth period of the periodic table. It has $3d^3$ configuration and crystallizes into bcc structure with a slightly bigger lattice constant than iron $a = 3.02 \text{ \AA}$ [57]. Bulk vanadium has the fourth highest critical temperature amongst the pure element superconductors ($T_C = 5.4 \text{ K}$ [57]). Its thin-film growth on Ir(111) substrate has never been published and so we did not have any relevant information on the preparation procedure. Before each vanadium deposition, the substrate was cleaned by the iridium cleaning procedure described in subsection 2.2.2.

After the degassing and calibration of the electron beam rod evaporator, we deposited approximately 20% of a monolayer on the clean substrate at room temperature without any post-annealing. The result is shown in Fig. 2.10a. We can see an iridium step of corresponding height and a homogeneously covered surface without any obvious preferential growth along the step edge. The islands have no defined shape. To trigger the surface diffusion and continuous film forming, we have tried to anneal the sample several times for short time (4 minutes). To check if any change occurs, we scanned the surface after each annealing. For each cycle we gradually increased the temperature from $390 \text{ }^\circ\text{C}$ to $550 \text{ }^\circ\text{C}$.

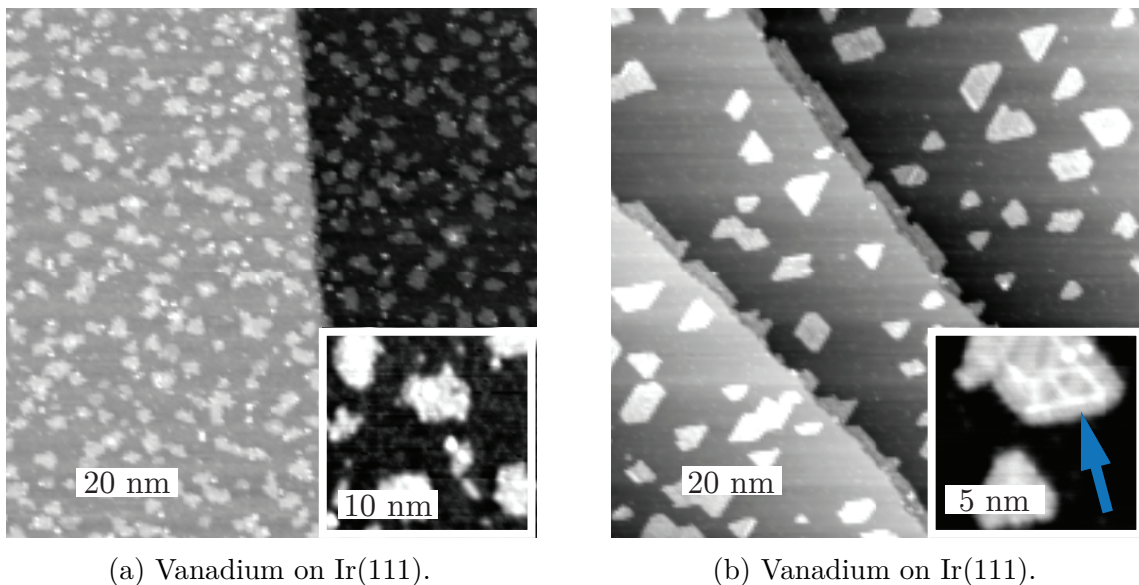


Figure 2.10: (a) Representative image of vanadium on the Ir(111) surface after deposition of $\sim 20\%$ of a monolayer at room temperature and no post annealing. The inset shows a zoom onto the surface. (Both $V_{\text{bias}} = 1 \text{ V}$, $I_{\text{setp}} = 500 \text{ pA}$) (b) Representative image of the same preparation after 4 minutes of annealing at $550 \text{ }^\circ\text{C}$. The height of the islands is $h = (1.44 \pm 0.12) \text{ \AA}$. The inset shows a zoom onto the island with visible structure (marked by the blue arrow). (Both $V_{\text{bias}} = 1 \text{ V}$, $I_{\text{setp}} = 500 \text{ pA}$)

After the last 4-minute annealing at $550 \text{ }^\circ\text{C}$, we observed a change of the surface appearance (presented in Fig. 2.10b). It shows polygonal islands with height of $h = (1.44 \pm 0.12) \text{ \AA}$ and sharp defined edges. On the iridium step edge we can see the growth of "wires" of the same height as the stand-alone islands. This means, that the annealing temperature was high enough to overcome the diffusion barrier. When zoomed closer on the island (inset of Fig. 2.10b), a bright structure can be seen in the topography image (marked by the blue arrow). Because vanadium and iridium have a different bulk

2. PREPARATION OF SUPERCONDUCTING-MAGNETIC INTERFACES

crystalline structures with different lattice constant, this structure could be caused by a strain relief of the vanadium film. To further investigate the growth properties of V on Ir(111) we decided to increase the coverage and deposit more vanadium.

As a next step, we deposited $\sim 40\%$ of a mono layer at the room temperature. For the post annealing, we used the same values that were sufficient to create flat islands for the lower vanadium coverage – 4 minutes at $550\text{ }^\circ\text{C}$. However, the effect on the islands was different (Fig. 2.11a). Although the islands shows some straight edges and sharp angular corners (marked by the yellow arrow), the surface is rather bumpy with the apparent height in the range of 0.8 \AA to 1.6 \AA . Along the step edges, only a small patches of vanadium are formed. But otherwise the surface is homogeneously covered and no major preferential diffusion towards the step edges can be observed. To improve the quality of the sample and to obtain a better vanadium islands, we have tried several short (4 minutes) sample annealing cycles, monitoring the state of the surface between each cycle. For each cycle, the annealing temperature was slightly increased, reaching $630\text{ }^\circ\text{C}$ for the last one. Unfortunately, the appearance of the surface and the islands was not improving and they exhibited the same surface roughness and even lost the polygonal shapes (not shown here).

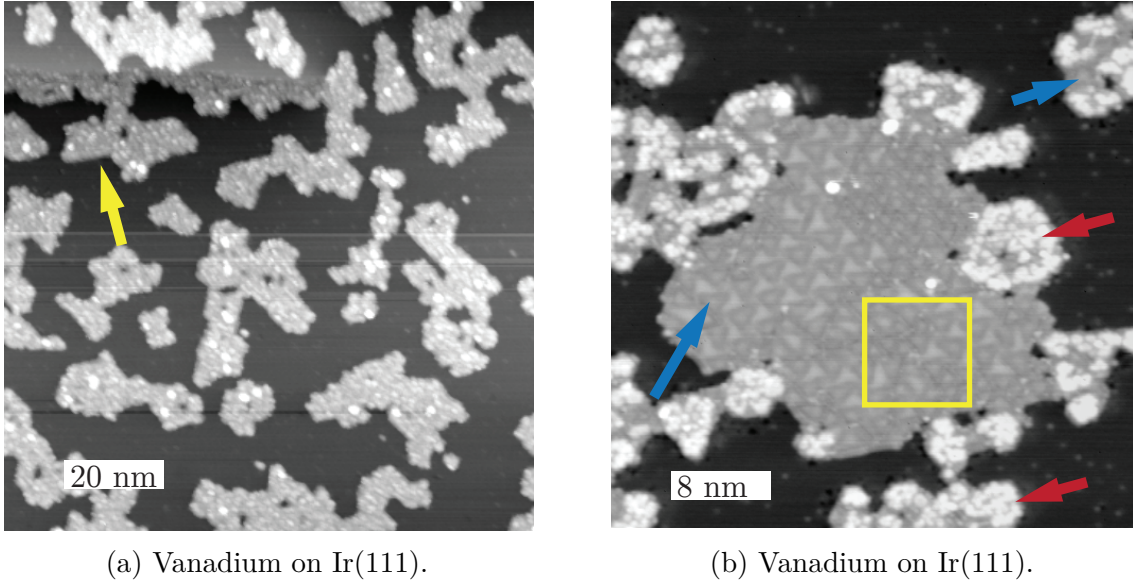
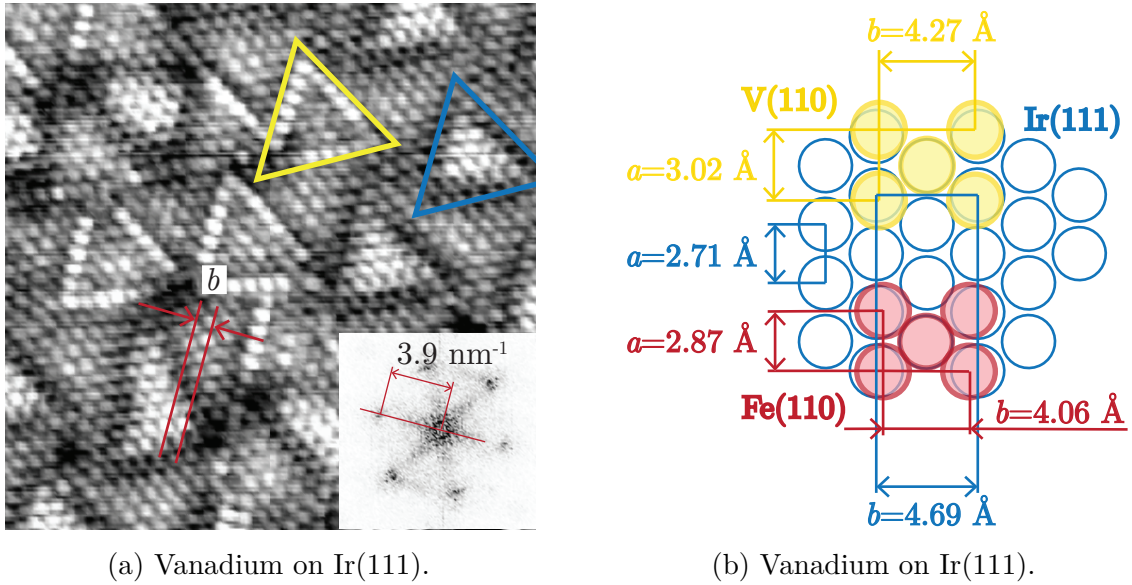


Figure 2.11: (a) Representative image of vanadium deposition ($\sim 40\%$ of a ML) at room temperature and 4 minutes post-annealing at $550\text{ }^\circ\text{C}$. Islands show sign of polygonal shaping, but do not form a flat film (yellow arrow). (b) Representative image of the same preparation after 30-minute annealing at $550\text{ }^\circ\text{C}$. The height of the "first layer" film (blue arrow) with visible superstructure is $h = (1.35 \pm 0.13)\text{ \AA}$. The "second layer" areas (red arrow) have a height around $h = 2\text{ \AA}$. (Both $V_{\text{bias}} = 1\text{ V}$, $I_{\text{setp}} = 500\text{ pA}$)

Our next step was to go back to the $550\text{ }^\circ\text{C}$ annealing temperature and anneal for a significantly longer time period – 30 minutes. The resulting STM images revealed islands, that were again polygon shaped with straight edges (Fig. 2.11b). They formed a visible flat "first layer" with a height of $h = (1.35 \pm 0.13)\text{ \AA}$ (relatively to the Ir(111) surface, marked by the blue arrow), which is comparable to the height of the low coverage islands in Fig. 2.10b. A significant area of the islands is in addition covered with bumps without any defined shape and a varying height around $h \approx 2\text{ \AA}$ (marked by the red arrow), forming thus a "second layer". The size of the island ($30 \times 30\text{ nm}$) and especially

the size of the clean "first layer" presented in Fig. 2.11b is not representative compared to the average size of the islands across the surface (mostly 10 nm wide). On this island, we can see a superstructure on the "first layer", that has a different pattern from the stripy structure visible on the low-coverage islands in Fig. 2.10b. This pattern is also visible on the other "first layers" islands on the surface.

Fig. 2.12a shows a zoom on the "first layer" surface with atomic resolution (the position of the zoom is marked on Fig. 2.11b by a yellow square). Atoms are ordered in a hexagonal threefold symmetry, just as the Ir(111) substrate. Besides the atoms, a triangular superstructure is visible with two types of apparent topography. The yellow arrow marks the triangular area with apparent higher edges than the centre of the triangle, whereas the blue arrow marks the area with apparent lower edges than the centre of the triangle. It can be noted, that on some edges of these triangles, the atomic rows are suddenly slightly shifted. For this reason, the 2D-FFT (shown in the inset, $k = 1/\lambda$ convention) is a bit fuzzy. However, from a statistical analysis we could determine the distance between the closest rows as $b = (2.58 \pm 0.35) \text{ \AA}$. This row span is comparable with the span of rows on the Ir(111) surface.



(a) Vanadium on Ir(111).

(b) Vanadium on Ir(111).

Figure 2.12: (a) Zoom image on the "first layer" vanadium island (position marked by the yellow square in Fig. 2.11b) with atomic resolution ($b = (2.58 \pm 0.35) \text{ \AA}$). The blue and yellow arrows mark a visible superstructure with two different appearances. The inset shows a 2D-FFT ($k = 1/\lambda$ convention) of the STM image. ($V_{\text{bias}} = 6 \text{ mV}$, $I_{\text{setp}} = 10 \text{ nA}$) (b) Simplified model of lattice mismatch between the V(110) plane (yellow), Fe(110) (red) plane and Ir(111) plane (blue).

To determine the origin of this superstructure would require a proper inspection, that was not a main goal of this project. A simple way to look at the pattern is to consider it as a strain relief structure. As shown previously, despite the lattice mismatch and different crystalline structure, iron grows pseudomorphically on Ir(111) in a fcc(111) lattice structure. In the second layer, a strain relief structure occurs. By comparing the distance between atoms, the dimensionally closest plane in bcc structure to the fcc(111) plane is bcc(110) plane. This is schematically illustrated in Fig. 2.12b. It shows the difference between the atom distance in the bcc Fe(110) plane (shown in red) and the atoms in fcc Ir(111) (shown in blue). If we define the atomic distances a and b as shown

2. PREPARATION OF SUPERCONDUCTING-MAGNETIC INTERFACES

in Fig. 2.12b, a 15.5 % stretch in b and a 5.6 % compression in a is necessary in order to adapt the Fe(110) plane to Ir(111) surface. In the case of V(110) (shown in yellow), the necessary deformation would be a 9.8 % stretch in b and a 10.2 % compression in a . For better comprehensibility, the distances a and b as well as deformation necessary to adapt the Fe(110) and V(110) planes to the Ir(111) plane are shown in Tab. 2.3.

Table 2.3: Summary of the distances a and b as defined in Fig. 2.12b as well as deformation required to adapt the Fe(110) and V(110) planes to the Ir(111) plane .

	a [Å]	compression [%]	b [Å]	stretch [%]
Ir	2.71	–	4.69	–
F	2.87	–5.6	4.06	15.5
V	3.02	–10.2	4.27	9.

Shape of the interaction-energy to atomic-distance curve shows a steeper increase of repulsion energy of metallic atoms when compressed together than increase of cohesive energy when stretched apart [60]. Based on this premise, we can qualitatively compare the calculated values for iron and vanadium. Due to the comparatively higher necessary compression of vanadium atoms in a , it is energetically harder to adapt to the V(110) plane to the Ir(111) substrate. Moreover vanadium ($E_C = 5.31$ eV/atom) has a higher cohesive energy than iron ($E_C = 4.28$ eV/atom) [61]. Building on these facts, we suggest that vanadium tends to grow pseudomorphically on Ir(111) just as iron. However, due to the larger lattice mismatch and higher cohesive energy, it is forced to adopt an energetically more stable position and to relieve the strain in the first layer. This can result to the formation of the observed structure in Fig. 2.10b and Fig. 2.12a.

Based on the presented results for the growth of vanadium on Ir(111), we could conclude, that vanadium does not tend to grow well in desired continuous and atomically flat patches. This is probably caused by a big lattice mismatch of both materials and strong cohesive energy between vanadium atoms. The goal of our project was, however, to primarily create a superconducting-magnetic interface. Therefore, we decided to first try vanadium growth on top of the pseudomorphic iron islands before investigating the next superconducting material, because due to a different interaction between V and Fe such growth could be different.

2.5. Growth of V on Fe-Ir(111)

Iron films on the clean Ir(111) surface as a substrate for the vanadium deposition were prepared exactly in the same way as described in section 2.3 with resulting wire-like formation of iron along the iridium step edges (Fig.2.8b).

From previous experiences we already knew that without additional annealing at 550 °C, vanadium does not overcome the diffusion barrier on iridium and does not grow in faceted islands. However, the diffusion behaviour for vanadium on iron could be different. Thus, for the first vanadium deposition on the Fe-Ir(111) interface, we evaporated about 40 % of a monolayer at the room temperature with no post-annealing. Indeed, Fig. 2.13 shows a different shape of the islands on the iron film than on the iridium terrace. The clusters located on iridium are comparably smaller and more scattered than the islands on the iron film, which are apparently bigger and all have similar sizes. The red arrows mark the distinguishable boundary between the iridium terrace and the iron film. Besides this,

a change in the height of the iron film relative to the iridium terrace occurred – while the height of the iron film on iridium before vanadium deposition was $h_{\text{Fe}} = (2.5 \pm 0.2) \text{ \AA}$ (Fig. 2.8b), now its apparent height decreased and is comparable to the height of iridium terrace $h_{\text{Fe}} = (2.1 \pm 0.3) \text{ \AA}$. We do not know the exact origin of this effect. One explanation could be a consequence of an electronic effect – the charge transfer between vanadium and iridium could be higher than the charge transfer between vanadium and iron. The iridium layer would be therefore electronically doped and as a result appear in average higher. The height of the iron film relative to the iridium surface would consequently decrease. Unfortunately, to confirm this suggestion, a proper charge transfer calculation would be necessary. Other plausible explanation would be, that the film is not pure iron any more, but a possible vanadium-iron alloy. However, when zoomed, the surface did not show any visible features, that would support this assumption.

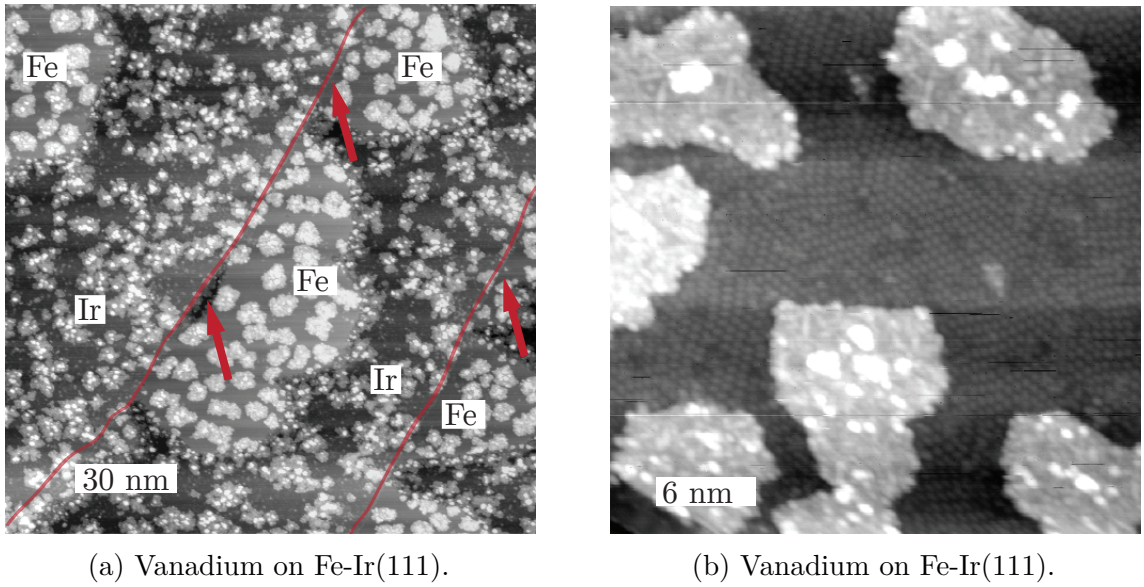


Figure 2.13: (a) Representative image of vanadium deposited on Fe-Ir(111) at room temperature without post annealing. An apparent difference in the size, shape and coverage of the clusters on iron film and iridium terrace can be seen. The red arrows show a distinguishable boundary between the iron and iridium – the apparent height of the iron film decreased to $h_{\text{Fe}} = (2.0 \pm 0.3) \text{ \AA}$ compared to the height of the iron film on iridium without vanadium $h_{\text{Fe}} = (2.5 \pm 0.2) \text{ \AA}$. (b) Representative image of assumed iron film with vanadium after 20 minutes annealing at $200 \text{ }^\circ\text{C}$. The surface between the clusters exhibits an ordered structure. The apparent height of this layer relative to the iridium terrace varies between $h = (1.7 \pm 0.2) \text{ \AA}$ (measured on the bright area) and $h = (1.4 \pm 0.2) \text{ \AA}$ (measured on the dark area). (Both $V_{\text{bias}} = 1 \text{ V}$, $I_{\text{setp}} = 500 \text{ pA}$)

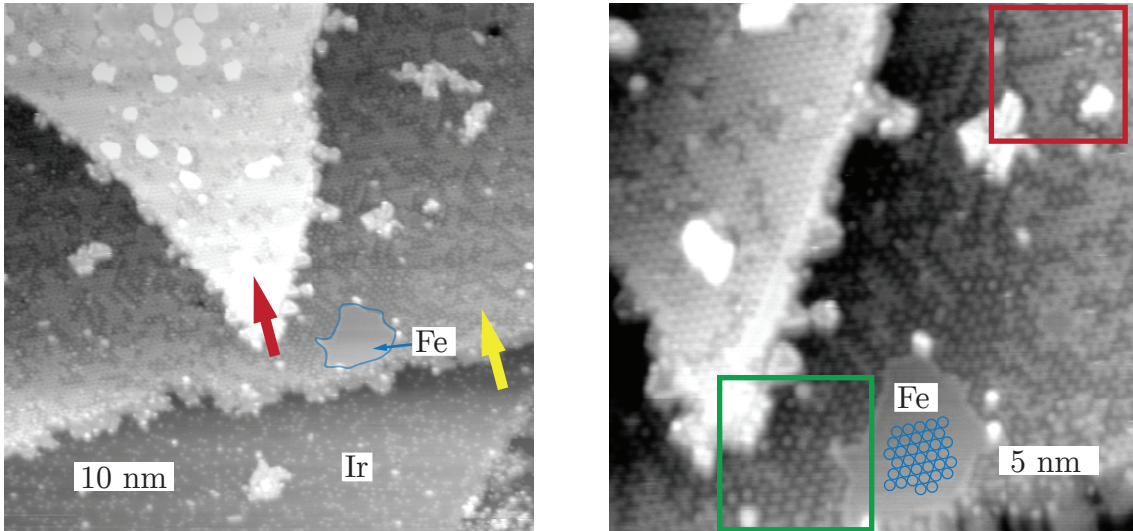
The annealing of the sample at $200 \text{ }^\circ\text{C}$ for 20 minutes did not change the overall appearance of the clusters on the iron film (comparable to Fig. 2.13). But when we zoomed on this area with vanadium covered iron film, we realized, that besides the clusters, the surface exhibited a highly ordered structure (presented in Fig. 2.13b). The apparent height of this layer relative to the iridium terrace varies between $h = (1.7 \pm 0.2) \text{ \AA}$ (measured on the bright area) and $h = (1.4 \pm 0.2) \text{ \AA}$ (measured on the dark area). From this behaviour we concluded, that vanadium on iron probably does not grow in flat continuous films as desired.

2. PREPARATION OF SUPERCONDUCTING-MAGNETIC INTERFACES

Nevertheless, if the visible ordered structure was not an alloy, but just a reconstruction of adsorbed vanadium on the iron film, it could modify the nanoskyrmion lattice. To further investigate its growth and a possible modification of the skyrmion lattice, we decided to deposit only a very small amount of vanadium. We wanted to reach such a low coverage, that the vanadium does not saturate the whole iron film (as in the case in Fig. 2.13b). It could then enable us to study the difference between the skyrmion lattice on the pure iron film and on the iron film with the reconstructed vanadium. Therefore we cleaned the substrate and made a new preparation of iron on iridium.

This time, we deposited only about 3% of a monolayer of vanadium at room temperature and did not anneal the sample afterwards. The result is shown in Fig. 2.14a. Besides iridium, that is clearly recognizable in the bottom part of the image, we can see two other layers of material (marked by the red and yellow arrows). On the middle layer (yellow arrow), there is a visibly clear and flat patch with apparent height $h = (2.0 \pm 0.1) \text{ \AA}$ relatively to the iridium surface (marked by blue arrow). This is comparable to the height of the assumed iron film without the reconstruction in Fig. 2.13.

When closer inspected (Fig. 2.14b), the middle layer shows two evident structural patterns. This was surprising, as on the high-coverage sample we found these structures only after the annealing to $200 \text{ }^\circ\text{C}$. The green square bounds the area with rows of elongated features (dotted structure), that look the same as observed on the preparation with higher coverage (Fig. 2.13b). The red square defines the area with a different honeycomb-like structure. We also managed to obtain an atomic resolution image on the flat patch of assumed iron, with hexagonal atomic lattice dimensionally consistent with iron in Fig. 2.9 (not shown here). Its orientation is indicated by the blue lattice drawing (not true to scale). Both structures seem to be aligned with the $\langle 011 \rangle$ directions of this assumed iron patch.



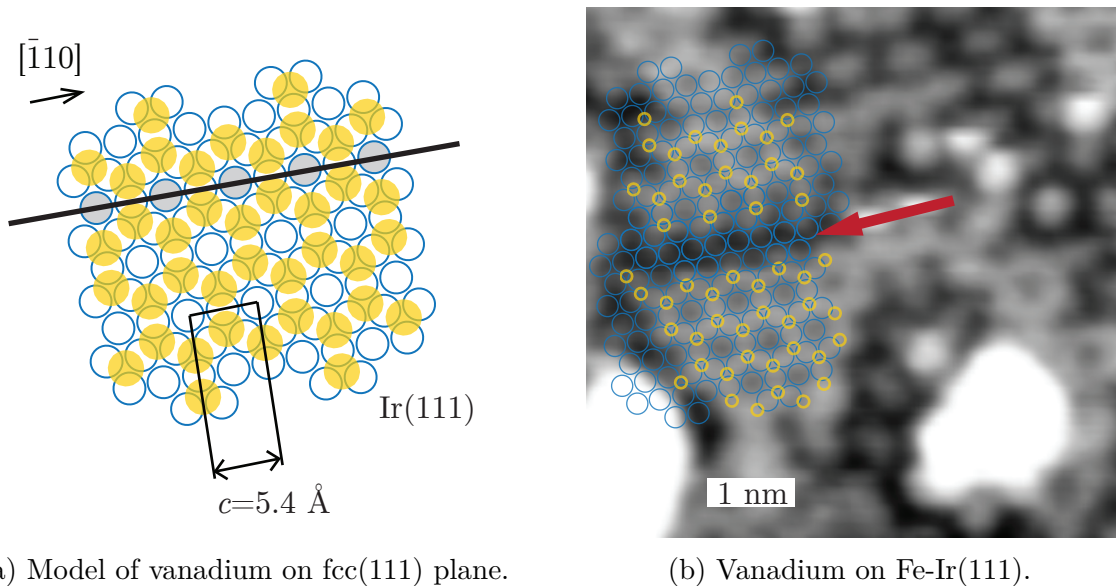
(a) Vanadium on Fe-Ir(111).

(b) Vanadium on Fe-Ir(111).

Figure 2.14: (a) Representative image of the low coverage vanadium on Fe-Ir(111). We can see two layers on the Ir(111) surface (marked by the red and yellow arrow). On the first layer is visible a flat patch with height $h = (2.0 \pm 0.1) \text{ \AA}$ (b) Zoom on (a). The surface shows two different structures – dotted structure (green square) and honeycomb structure (red square). The drawing of the blue lattice shows the orientation of atoms in the flat patch of assumed iron (not true to scale). (Both $V_{\text{bias}} = 1 \text{ V}$, $I_{\text{setp}} = 500 \text{ pA}$)

As already mentioned, no literature could be found on V-Fe-Ir(111) systems. Nevertheless, Surnev *et al.* [62] showed a study on the growth of an ultrathin vanadium oxide layer on Pd(111). They presented STM and LEED results supported by DFT calculations in which vanadium atoms are arranged in honeycomb-like structure on Pd(111) and the oxygen atoms are located as a top most layer on the vanadium. Since the oxygen atoms in this study are arranged atop of vanadium, they should not markedly affect the arrangement of vanadium on Pd(111).

The Ir(111) (pseudomorphic Fe(111) as well) and Pd(111) planes are dimensionally almost identical [57], we tried to construct a similar reconstruction (without oxygen) on such an fcc(111) surface as shown in Fig. 2.15a. The vanadium atoms occupy hollow positions on the Ir(111) plane, thereby forming a honeycomb-like structure. The span between the two closest centres of the hexagons is calculated from the Ir(111) plane dimensions as $c = 5.4 \text{ \AA}$ (twice the closest atom distance). It can be noted that the rows of the honeycomb centres follow the $\langle 011 \rangle$ directions on the Ir(111) plane.



(a) Model of vanadium on fcc(111) plane.

(b) Vanadium on Fe-Ir(111).

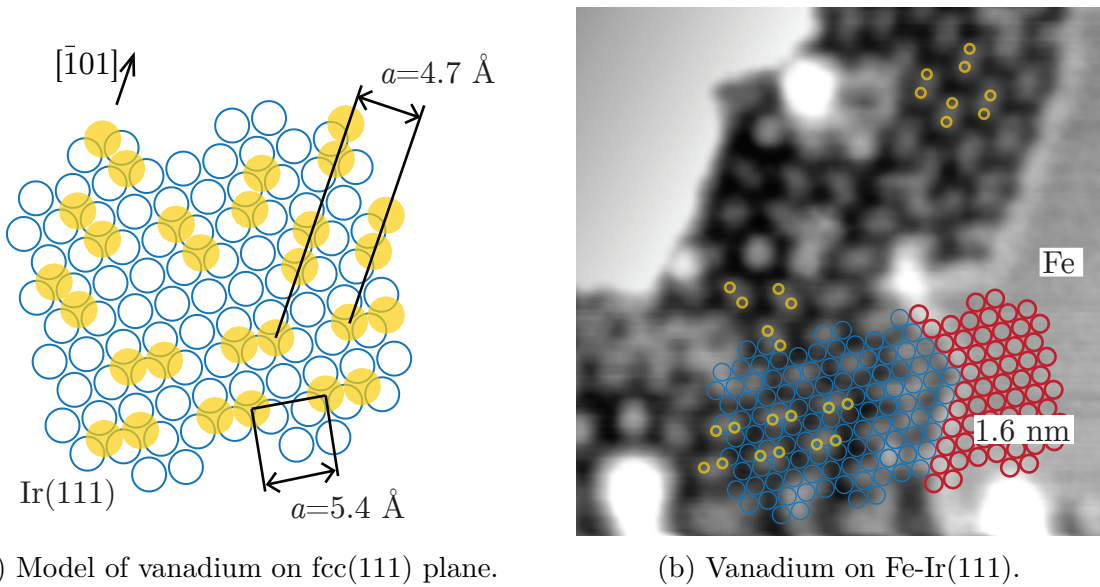
Figure 2.15: (a) Model of vanadium honeycomb-like reconstruction on Ir(111) plane. Blue circles represent the Ir(111) plane and the yellow circles, located on the hollow sites, represent the vanadium atoms. The theoretical distance between the closest centres of the honeycombs is $c = 5.4 \text{ \AA}$. (b) Fit of the presented model into the real structure in the STM image. The measured distance between the centres of the honeycombs is $c = (5.4 \pm 0.2) \text{ \AA}$ and the orientation of the structure corresponds to the orientation of the hexagonal lattice measure on the assumptive flat patch of Fe in Fig. 2.14b. ($V_{\text{bias}} = 1 \text{ V}$, $I_{\text{setp}} = 500 \text{ pA}$)

It turned out that by superimposing this structure over the STM image and scaling it to the corresponding dimensions, the proposed structure fits very nicely to the real observed features (Fig. 2.15b). The distance between the centres of honeycombs in the image is $(c = 5.4 \pm 0.2) \text{ \AA}$, which is in perfect agreement with the theoretical value. Moreover, the orientation of the fcc(111) substrate is in agreement with the angle of the hexagonal lattice measured on the flat patch as shown in Fig. 2.14b. There is a visible phase boundary on the STM image between the two phases of the honeycomb structure (marked by the red arrow). This is also in agreement with the modelled structure, when

2. PREPARATION OF SUPERCONDUCTING-MAGNETIC INTERFACES

the two phases are shifted relatively to each other on the same extended fcc (111) substrate lattice as demonstrated in the image.

For the dotted structure, that consisted of elongated features, we could not find any literature reference. This structure appears in the image oriented in three directions, that are rotated by 60° with respect to each other. This resembles a threefold symmetry and could suggest the orientation of the elongated features on the fcc(111) along the $\langle 011 \rangle$ directions. The apparent elongation could be a result of two atoms sitting on the neighbouring hollow sites. Based on these assumptions, we proposed a reconstruction presented in Fig. 2.16a. Here the tight pairs of vanadium atoms are located on the hollow sites in rows along the $\langle 011 \rangle$ directions with two iridium interatomic distances between them $b = 5.4 \text{ \AA}$. The next row, that is located within the distance $a = 4.7 \text{ \AA}$ (corresponds to the double distance of the closest atomic rows) is asymmetrically shifted lengthwise by one iridium interatomic distance.



(a) Model of vanadium on fcc(111) plane.

(b) Vanadium on Fe-Ir(111).

Figure 2.16: (a) Model of the vanadium atom-pair reconstruction on fcc(111) plane. Blue circles represent the fcc(111) plane and the yellow circles, located on the hollow sites, represent the vanadium atoms. The theoretical distance between the rows is $a = 4.7 \text{ \AA}$ and the distance between the pairs lengthwise is $b = 5.4 \text{ \AA}$. (b) The fit of the presented model into the real structure on the STM image. The measured distance between the rows is $a = (4.9 \pm 0.3) \text{ \AA}$ and the distance between the elongated features is $b = (5.6 \pm 0.2) \text{ \AA}$. The orientation of the structure corresponds to the orientation of the hexagonal lattice measured on the flat patch of assumed iron (red part of the lattice model). ($V_{\text{bias}} = 1 \text{ V}$, $I_{\text{setp}} = 500 \text{ pA}$)

The graphical fit to the measured data is presented in Fig. 2.16b. We can fit the proposed structure to all three orientations, with the scale corresponding to the scale of the image. The distance between the rows in each direction is $a = (4.9 \pm 0.3) \text{ \AA}$ and the distance between the elongated features lengthwise is $b = (5.6 \pm 0.2) \text{ \AA}$. Both values are consistent with the theoretically calculated value. Remarkable is a precise congruence of the modelled fcc(111) substrate with the orientation of the hexagonal lattice in the flat iron patch (shown in red lattice model) and also its resemblance with the shape of this patch. At some points in the STM image, however, the suggested structure does not agree completely with the measured data and features are shifted, stretched or compressed

relative to the proposed model structure. Unfortunately, we could not find a sufficiently big area with undisrupted structure to try the graphical superimposition over longer distances.

The question now is whether the reconstruction is vanadium on Ir(111), vanadium on Fe(111) or an alloy of these materials. Both suggested reconstructions can be located either on Ir(111) or on the pseudomorphic Fe(111) film, that have both the same lattice dimensions. In the first case the iron had to be pushed away by the vanadium except for the flat patch of assumed iron visible in all images. The vanadium would then be positioned on the Ir(111) as suggested, next to the flat pseudomorphic Fe(111) patch. In the second case, the iron stays on the same wire-like location as before the deposition and the pseudomorphic Fe(111) film is covered with the vanadium as suggested. But because the coverage is low, it can not saturate the whole surface and a clear patch of iron can be visible in the images. The height of the first layer, where both reconstructions can be seen, varies from 1.4 Å to 1.9 Å relative to the iridium terrace, depending on whether we measure on the bright or dark features. The reconstructed layer therefore appears like being positioned next to the flat patch of assumed iron. This could point more to the first proposed case, but since the STM image is always a combination of a real topography and electronic structure it is impossible without additional investigation to determine the true nature of the reconstruction. It would include more deeper STM and STS statistics, DFT calculations and gaining of additional informations by other surface sensitive techniques as LEED or Auger spectroscopy.

To sum up, we have found out, that vanadium does not grow in a flat and continuous film neither on Ir(111) nor on the Fe-Ir(111) substrate, which means the superconductivity in the thin film limit would not be preserved. For this reason it can not be used as a superconducting component of the desired superconducting-magnetic interface. Further, we observed small patches of two types of possible vanadium reconstruction on the Fe-Ir(111). We suggested a reconstruction model, that fits to the measured data. However, we did not manage to control the growth of either type in a larger continuous patch. A further and deeper investigation would be necessary to determine the true nature of the observed structure and mechanism of its growth. If the vanadium reconstruction on iron film (with nanoskyrmion lattice) would be confirmed, its controlled growth in larger continuous patches could have an interesting impact on the nanoskyrmion lattice.

2. PREPARATION OF SUPERCONDUCTING-MAGNETIC INTERFACES

3. Magnetism of Co atoms on WS₂

This chapter provides a brief overview on the study of magnetic properties of cobalt atoms on a monolayer dichalcogenide WS₂. In the first section, the basic principles of X-ray circular magnetic dichroism (XMCD) are explained. The second section provides insight into the investigated system of Co atoms on WS₂/Au(111) and in the last section, the first qualitative results of XMCD spectra with respect to the magnetic anisotropy of cobalt atoms are presented.

3.1. X-ray circular magnetic dichroism (XMCD)

The absorption of photons is a basic principle of some of the most effective spectroscopy methods, because its mechanism is governed by simple electronic dipole transitions. To probe the atomic core levels, X-ray photoelectron spectroscopy (XPS) and X-ray absorption spectroscopy (XAS) are the two most utilized techniques. Use of the latter technique enables measurement of energy dependent x-ray absorption spectra with characteristic resonance peaks. These peaks originate from transitions of core electrons to unoccupied valence band states. The $3d$ band transition metals are best probed using $2p \rightarrow 3d$ transitions, because the electron transitions are guided by the $\Delta l = \pm 1$ selection rule. [63, 64]

To study the size and the direction of the electron angular momentum and spin in the sample, a circularly polarized synchrotron radiation is used. The right-circularly-polarized (RCP) photons have the electric field vector \mathbf{E} rotating clockwise around the wave vector \mathbf{k} when viewed in the direction of \mathbf{k} . These photons have an angular momentum of $+\hbar$ and can be described by a vector – the photon spin. On the other hand, the left-circularly-polarized (LCP) photons have an angular momentum of $-\hbar$ with the photon spin in the opposite direction and their electric field vector rotates in the anticlockwise sense. The XMCD signal is defined as difference between the X-ray absorption spectra for RCP and LCP light. [63, 64]

Developed by Schütz *et al.* [65], the XMCD principle for a $3d$ transition metal (for example cobalt) is depicted in Fig. 3.1. Here the inequality of spin-up and spin-down electrons (or equivalently spin-up and spin-down holes above the Fermi level) below the Fermi energy (E_F) is supposed, which gives the $3d$ shell a net spin moment. Transfer of the angular momentum of photons, $+\hbar$ and $-\hbar$, to the $2p$ core level electrons by using the RCP and LCP x-rays makes the absorption process dependent on the core electron spin and thus enables measurement of the difference in the number of $3d$ holes with spin-up and spin-down orientation. For the spin-orbit-split levels, e.g $2p_{1/2}$ (L_2 edge) and $2p_{3/2}$ (L_3 edge), the angular momentum of the photon is transferred partially to the spin via the spin-orbit coupling.

3. MAGNETISM OF CO ATOMS ON WS₂

The photoexcited electron can carry both spin and angular momentum. Photoexcited electrons with opposite spins can be created, because RCP, respectively LCP, photons transfer the momentum of the opposite direction. Since the flipping of the spin during the transition is forbidden, photoexcited electron with spin-up orientation from the $2p$ level can be transitioned only into a spin-up hole in the $3d$ state and vice versa for the spin-down photoelectrons. The absorption intensity is therefore directly proportional to the number of available states of given spin in the $3d$ valence shell, that acts as a spin sensitive detector. [63, 64]

The magnetization direction determines the quantization axis of the $3d$ shell during the experiment and the dichroism effect is proportional to the cosine of the angle Θ between the magnetization direction and the photon spin. Therefore, the maximum signal is obtained for the antiparallel and parallel orientations of the sample magnetization with respect to the photon spin [63, 64]. The projections of the spin and magnetic orbital moments per hole in the d-shell can be quantitatively obtained via the XMCD sum rules for differences in absorption intensities for the parallel and antiparallel orientations of the sample magnetization direction and the incoming photon spin [11].

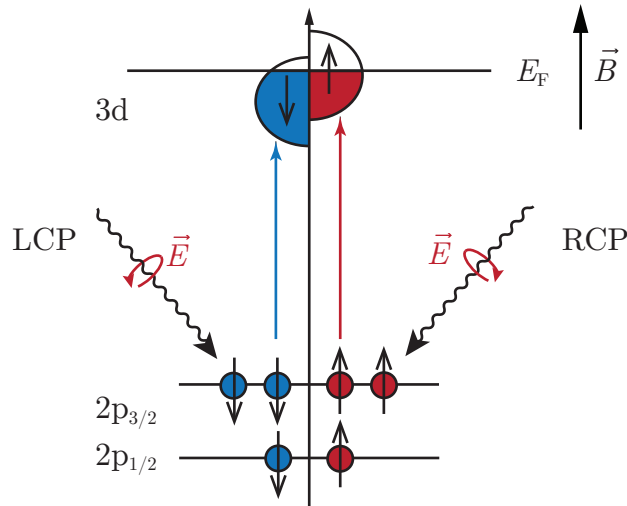


Figure 3.1: Schematic drawing of the XMCD principle for the L edge absorption between $2p$ core levels and $3d$ valence shell of transition metals (e.g. cobalt). The spin-up (spin-down) photoelectrons are excited primarily by the RCP light (LCP light). The obtained absorption intensity is directly proportional to the number of empty $3d$ shell states of a given spin, because the flipping of the spin is forbidden.

In a magnetically anisotropic material, the magnetic moment tends to align along an energetically favourable direction, a so-called easy axis. The anisotropy describes how much the magnetisation orientation of material responds to the thermal or magnetic stimuli. The magnetic anisotropy energy (MAE) is a material property, that represents the energy necessary to change the magnetization direction from the easy axis to the unfavourable direction with the maximum ground energy (hard axis). Measuring XMCD along an easy axis will show more pronounced spectral peak, contrary to the measurements along hard axes. As a consequence, if the measured sample exhibits magnetic anisotropy, the XMCD spectra for different non-parallel directions will show different intensities [11].

In actual measurements superconducting magnets are used, since strong magnetic fields are required in order to magnetize the sample along both the easy and hard axes.

3.2. Motivation and sample preparation

Magnetic materials assume an important part in present data storage innovation and industry. For many applications, the magnetic anisotropy of the materials defines their suitability and efficiency. The magnetic anisotropy is a consequence of a connection between the spin magnetization and the atomic structure of the magnetic material, mediated by the spin-orbit interaction [66]. Gambardella *et al.* [11] presented a study on magnetism of single cobalt atoms deposited onto the non-magnetic Pt(111) substrate. Their experiment revealed, that whereas the free gas-phase cobalt atoms have, according to Hund's rules, large spin (\mathbf{S}) and orbital (\mathbf{L}) magnetic numbers and no magnetic anisotropy (because of the spherical symmetry), a giant magnetic anisotropy appears as the atoms are deposited onto the Pt (111) substrate. Gambardella *et al.* [11] showed a big increase of the cobalt adatom \mathbf{L} compared to the bulk orbital moment and explained it as a consequence of the reduced coordination of the cobalt adatom adsorbed atop the surface. The reduced coordination supports d-electron localization and preservation of atomic-like character in the 3d orbitals.

The large magnetic anisotropy of the above mentioned system is a combination of different effects [11, 66]:

1. the reduced symmetry of adsorbed Co atoms in comparison to the gas-phase atoms, that provides the required condition to show anisotropic behaviour,
2. localisation of 3d electrons that enlarge the spin-orbit energy due to an increase in \mathbf{S} and prevents the quenching of the orbital moment,
3. strong spin-orbit splitting of the 5d platinum states.

The angular dependence of the magnetic anisotropy is governed mainly by the 1. effect, while the magnitude of the magnetic anisotropy energy is determined by the 2. and 3. effects [11].

3.2.1. WS_2

Stable monolayers of solids have been investigated since the discovery of graphene [67]. It was soon realized, that other bulk materials with layered structure can be mechanically exfoliated to form monolayers a monolayers of 2D materials – among others, also transition metal dichalcogenides (TMDCs). Electronic properties of single-layer TMDCs are modified compared to the bulk material – for example in the case of MoS_2 [68], a transition from the indirect to the direct band gap is observed.

Denzik *et al.* [69] introduced an epitaxial growth method for another TMDC – WS_2 on Au(111), that provides a high quality single-layer WS_2 . Like the other TMDCs, tungsten disulfide consists of a layer of tungsten sandwiched between two sulphur layers. Denzik *et al.* [69] showed a study of various properties of single-layer WS_2 on Au(111) by STM, LEED, core level spectroscopy and ARPES. It was found out, that due to the lattice mismatch between the single-layer WS_2 and the substrate, the modulation of the local density of states occurs and a consequent Moiré pattern is observed. Furthermore, when

3. MAGNETISM OF CO ATOMS ON WS₂

probing the electronic structure by ARPES, Dendzik et *al.* [69] measured a strong spin-splitting around the \bar{K} point, almost three times bigger than the spin-splitting in single-layer MoS₂ [68]. The ARPES data also confirmed the expected direct band-gap at \bar{K} for the single-layer WS₂ as opposed to the multilayer case.

3.2.2. Sample preparation – Co on WS₂

If used as a substrate, the strong spin-orbit coupling (SOC) of the tungsten in WS₂ could be favourable for augmenting the magnetic anisotropy of Co adatoms as was shown by Gambardella et *al.* [11]. However, since WS₂ is sandwich-structure material and the topmost layer is sulphur, this effect would strongly depend on the position of Co adatoms – one possibility is that Co relaxes between the first 2 layers where it could feel the large SOC of tungsten. Besides, since the single-layer WS₂ was reported to possess a direct band gap, it could be attractive for electronic applications. This makes the single-layer WS₂ a suitable candidate for measuring the magnetic anisotropy of cobalt atoms, similarly to the Gambardella et *al.* [11] study.

The single-layer WS₂/Au(111) samples were prepared the same way as shown by Dendzik et *al.* [69] by evaporation of tungsten onto the clean Au(111) substrate with simultaneous exposure to H₂S. Afterwards, the samples were post-annealed in the H₂S atmosphere. The quality of the samples was checked by STM and XPS prior to XAS measurements (not shown here).

The Co atoms were deposited by electron beam evaporator in UHV conditions onto the clean WS₂/Au(111) substrate. To inhibit surface diffusion and preserve the isolated atom character, the deposition was carried out at $T \sim 2$ K. The deposition rate was calibrated on a clean Au(111) substrate by STM imaging (not shown here).

3.3. First results

To obtain information about the magnetization of Co adatoms on WS₂/Au(111), the XAS spectra at the L_3 edge with RCP and LCP x-rays were measured in the total electron yield mode (shown in Fig.3.2). The measurements were performed at $T \sim 2$ K and to magnetize the sample, a $B = 6$ T field was used at angles $\Theta = 0^\circ$ and $\Theta = 60^\circ$ with respect to the surface normal. The XMCD spectra was obtained as a difference between the absorption spectra measured for the parallel μ_+ and antiparallel μ_- alignment of the incoming photon helicity with the applied field \mathbf{B} .

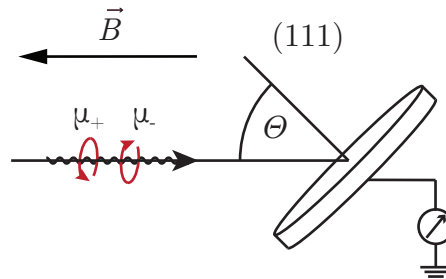


Figure 3.2: Schematic drawing of a XAS experimental set-up in the total electron yield mode. The sample was exposed successively to the RCP and LCP light. A $B = 6$ T magnetic field was used at angles $\Theta = 0^\circ$ (out-of-plane magnetization) and $\Theta = 60^\circ$ (in-plane magnetization) with respect to the surface normal.

In-depth analysis of the measured XMCD data is still in process and therefore only first qualitative results will be shown here. In total, four samples have been investigated, but due to problems with the experimental set-up, we managed to measure meaningful spectra for both in-plane and out-plane magnetization only on one of them. All data shown here were measured on this sample with $\sim 7\%$ of a monolayer coverage.

The normalized XAS spectra for $\Theta = 0^\circ$ (out-of-plane magnetization) and $\Theta = 60^\circ$ (in-plane magnetization) are presented in Fig.3.3. The $\Theta = 60^\circ$ signal is for better comprehensibility shifted up by 0.01 arb.u.. The signal shows relatively weak absorption L_3 resonance peaks in comparison with the substrate background – about $\sim 0.25\%$ for the $\Theta = 0^\circ$ orientation and $\sim 0.4\%$ for the $\Theta = 60^\circ$ orientation. All spectra also show an artefact peak of unknown origin at $E = 783.2$ eV. We can see that there is no big difference between the μ_+ and μ_- for both sample magnetization orientations and therefore the dichroism is very weak. Moreover, there is no strong anisotropy in the XAS lineshapes, which suggests that crystal field effects from neighbouring atoms, e.g. negatively charged sulphur atoms, are possibly weak.

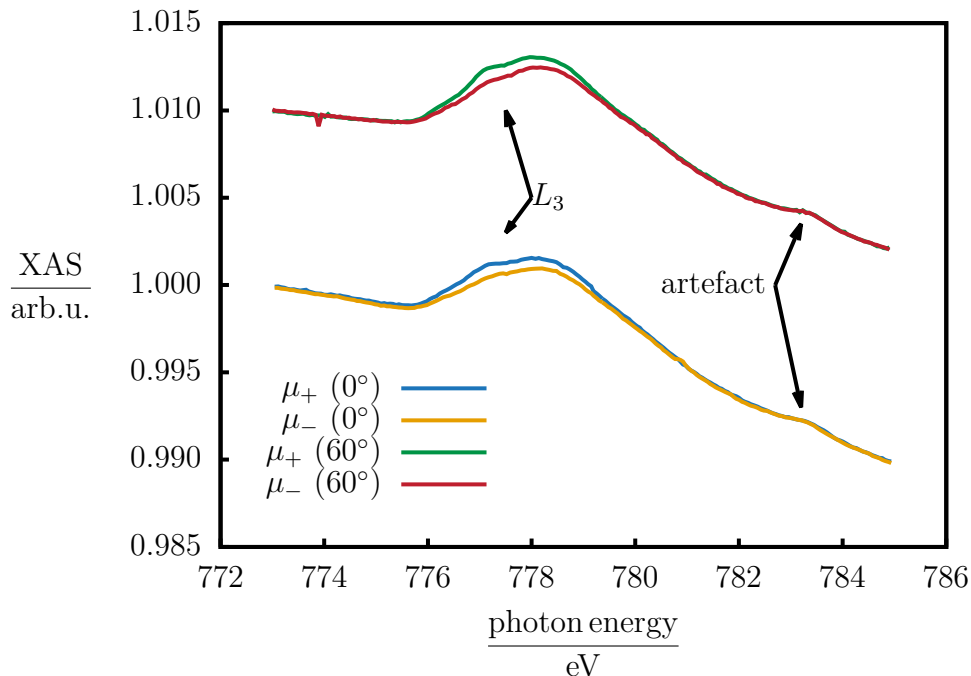


Figure 3.3: Normalized XAS spectra of $\sim 7\%$ ML Co on $\text{WS}_2/\text{Au}(111)$ for the parallel μ_+ and antiparallel μ_- alignment of the incoming photon helicity with \mathbf{B} at $\Theta = 0^\circ$ (out-of-plane magnetization) and $\Theta = 60^\circ$ (in-plane magnetization) relative to the surface normal. Spectra were measured at $T \sim 2$ K for $B = 6$ T. The $\Theta = 60^\circ$ signal is shifted up by 0.01 arb.u. for a better comprehensibility. In both spectra a L_3 edge jump can be seen - about $\sim 0.25\%$ for the $\Theta = 0^\circ$ and $\sim 0.4\%$ for the $\Theta = 60^\circ$. At $E = 783.2$ eV a small artefact peak of unknown origin can be seen.

The subtracted μ_+ and μ_- signals for both magnetization orientations exhibit weak XMCD spectra with a $\sim 30\%$ XMCD/XAS ratio for $\Theta = 0^\circ$ and $\sim 20\%$ XMCD/XAS ratio for $\Theta = 60^\circ$ (shown in Fig.3.4). Also, the XMCD spectra do not exhibit any significant difference for the in-plane and the out-of-plane magnetization.

As was mentioned, three other samples were measured and the in-depth analysis of the obtained data is still in process and beyond the scope of this work. As a first result how-

3. MAGNETISM OF CO ATOMS ON WS₂

ever, based on the presented data we concluded that there is no obvious strong magnetic anisotropy of cobalt atoms on WS₂/Au(111) substrate. Thus, there is no preferential in-plane or out-of-plane orientation of the cobalt's magnetic moment, as suggested already by the weak anisotropy in the XAS lineshape. This finding is in contrast to the Gambardella *et al.* [11] study on the Co/Pt(111) system, where a strong out-of-plane magnetization of Co adatoms has been observed. This is not very surprising since, as mentioned, the effect strongly depends on the position of Co atoms on the substrate. E.g. if the Co atom sits bounded by Van der Waals interaction only atop of the sulphur layer, it possibly can not feel the strong SOC of tungsten. This is planned to be probed by LT-STM, to find out how much the Co atoms "sink" into the topmost sulphur layer.

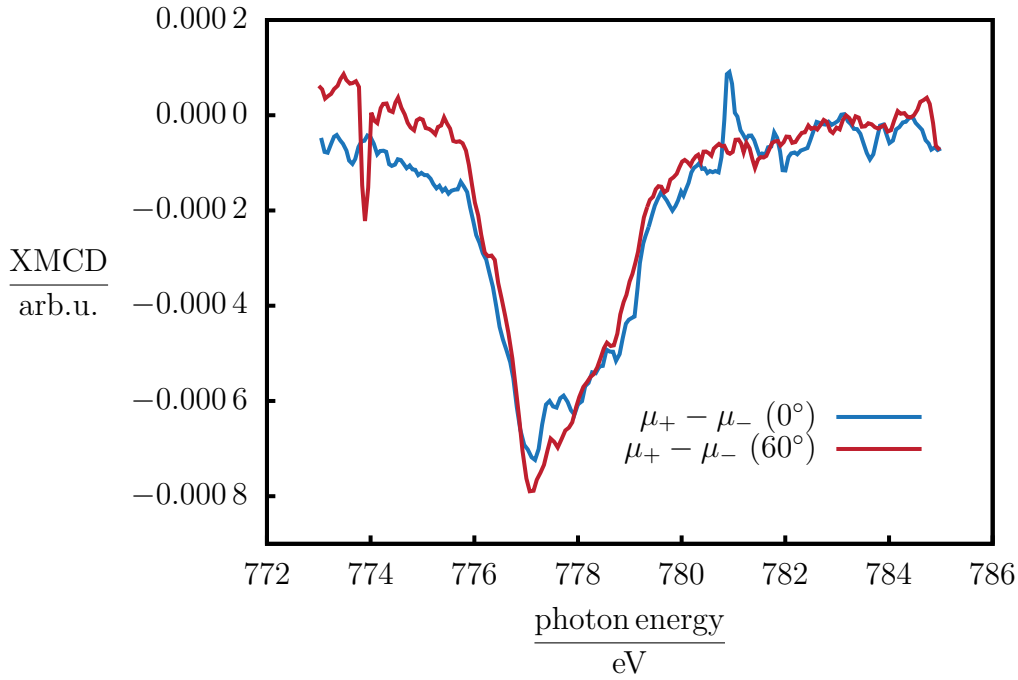


Figure 3.4: XMCD spectra $\mu_+ - \mu_-$ of $\sim 7\%$ ML Co on WS₂/Au(111). No significant difference in the spectra measured for $\Theta = 0^\circ$ and $\Theta = 60^\circ$ magnetization directions can be observed.

Summary and outlook

LT-STM study As a first stage in the course of this work, Omicron LT-STM experimental set-up was refurbished. To improve the short standing time of the liquid bath cryostat, two main modifications have been carried out. The radiation shielding was adjusted to transmit less radiation from outside and by redesigning the former Omicron wiring layout, we managed to significantly decrease the thermal bridging of the STM stage to the room temperature environment. Due to these modifications, we managed to double the cryostat standing time on LHe temperature from 19 h to 40 h. As a second part of the refurbishment, we changed the electronic control unit and the signal amplifier. The improvement was checked by test measurements on Au(111) crystal (spectroscopy of Shockley surface state) and Pb(111) (spectroscopy of superconducting gap).

In the refurbished experimental set-up, we tried to adapt known methods for cleaning W(110) and Ir(111) crystals. We observed and analysed an oxygen and carbon reconstruction on W(110) during different phases of the cleaning. This helped us to recalibrate our pyrometer temperature reading. In the case of Ir(111), the efficient cleaning procedure was reached without major problems and we managed to grow pseudomorphic thin Fe layers along the step edges on the Ir(111) substrate. The pseudomorphic growth was confirmed by comparison of atomic resolution images on both Fe layers and clean Ir(111). We did not succeed in growing high quality thin vanadium films on Ir(111) because of strain relief structures induced by a big lattice mismatch between the film and the substrate. Equally, the deposition of vanadium onto the Fe thin films on Ir(111) did not result in desired growth. Instead, we observed two different types of surface reconstructions of V on Fe/Ir(111) and suggested a possible reconstruction geometry. Deeper investigation of these reconstructions was beyond the scope of this work.

All in all, this project was part of a long-term research aiming to prepare a stable superconducting-magnetic interface. It contributed in developing an efficient substrate preparation method and in testing of the thin vanadium films growth. The plan in the near future is to investigate the growth of thin films on Fe/Ir(111) made of other materials as niobium, tantalum, aluminium and lead.

XMCD study Because the in depth analysis of the measured data is still in process, only first qualitative results of XMCD on the investigated Co/WS₂/Au(111) system have been presented. It was shown, that the XMCD signal for both in-plane and out-of-plane magnetization is very weak and therefore no strong anisotropy of single Co atoms on WS₂/Au(111) can be expected. This behaviour could be dependent on the position of Co atoms on the WS₂ layer. Therefore, a further LT-STM investigation is planned to provide supplemental information.

SUMMARY AND OUTLOOK

References

- [1] KRAUSE, S., L. BERBIL-BAUTISTA, G. HERZOG, M. BODE and R. WIESENDANGER. Current-Induced Magnetization Switching with a Spin-Polarized Scanning Tunneling Microscope. *Science*. 2007, vol. 317, pp. 1537–1540. Available from: doi:10.1126/science.1145336.
- [2] BERGMANN, K., S. HEINZE, M. BODE, E. Y. VEDMEDENKO, G. BIHLMAYER, S. BLÜGEL and R. WIESENDANGER. Observation of a Complex Nanoscale Magnetic Structure in a Hexagonal Fe Monolayer. *Phys. Rev. Lett.* 2006, vol. 96, pp. 167–203. Available from: doi:10.1103/PhysRevLett.96.167203.
- [3] HEINZE, S., K. BERGMANN, M. MENZEL, J. BREDE, A. KUBETZKA, R. WIESENDANGER, G. BIHLMAYER and S. BLUGEL. Spontaneous atomic-scale magnetic skyrmion lattice in two dimensions. *Nat Phys*. 2011, vol. 7, pp. 713–718. Available from: doi:10.1038/nphys2045.
- [4] KHAJETOORIANS, A., J. WIEBE, B. CHILIAN, S. LOUNIS, S. BLUGEL and R. WIESENDANGER. Atom-by-atom engineering and magnetometry of tailored nanomagnets. *Nature Physics*. 2012, vol. 8, pp. 497–503. Available from: doi:10.1038/nphys2299.
- [5] DELACOUR, Cécile, Luc ORTEGA, Marc FAUCHER, Thierry CROZES, Thierry FOURNIER, Bernard PANNETIER and Vincent BOUCHIAT. Persistence of superconductivity in niobium ultrathin films grown on R-plane sapphire. *Phys. Rev. B*. 2011, vol. 83, pp. 144504. Available from: doi:10.1103/PhysRevB.83.144504.
- [6] EOM, Daejin, S. QIN, M.-Y. CHOU and C. K. SHIH. Persistent Superconductivity in Ultrathin Pb Films: A Scanning Tunneling Spectroscopy Study. *Phys. Rev. Lett.* 2006, vol. 96, pp. 027005. Available from: doi:10.1103/PhysRevLett.96.027005.
- [7] NADJ-PERGE, Stevan, Ilya K. DROZDOV, Jian LI, Hua CHEN, Sangjun JEON, Jungpil SEO, Allan H. MACDONALD, B. Andrei BERNEVIG and Ali YAZDANI. Observation of Majorana fermions in ferromagnetic atomic chains on a superconductor. *Science*. 2014, vol. 346, pp. 602–607. Available from: doi:10.1126/science.1259327.
- [8] BODE, M., R. PASCAL and R. WIESENDANGER. STM study of carbon-induced reconstructions on W(110): strong evidence for a surface lattice deformation. *Surface Science*. 1995, vol. 344, pp. 185–191. Available from: doi:http://dx.doi.org/10.1016/0039-6028(95)00873-X.
- [9] ZAKERI, Kh., T.R.F. PEIXOTO, Y. ZHANG, J. PROKOP and J. KIRSCHNER. On the preparation of clean tungsten single crystals. *Surface Science*. 2010, vol. 604, pp. L1–L3. Available from: doi:http://dx.doi.org/10.1016/j.susc.2009.10.020.

REFERENCES

- [10] BODE, M., S. KRAUSE, L. BERBIL-BAUTISTA, S. HEINZE and R. WIESEN-DANGER. On the preparation and electronic properties of clean W(1 1 0) surfaces. *Surface Science*. 2007, vol. 601, pp. 3308–3314. Available from: doi:<http://dx.doi.org/10.1016/j.susc.2007.06.017>.
- [11] GAMBARDELLA, P., S. RUSPONI, M. VERONESE, S. S. DHESI, C. GRAZIOLI, A. DALLMEYER, I. CABRIA, R. ZELLER, P. H. DEDERICHS, K. KERN, C. CARBONE and H. BRUNE. Giant Magnetic Anisotropy of Single Cobalt Atoms and Nanoparticles. *Science*. 2003, vol. 300, pp. 1130–1133. Available from: doi:[10.1126/science.1082857](https://doi.org/10.1126/science.1082857).
- [12] SOURCE, Diamond Light. *I06: Nanoscience, X-ray Magnetic Circular Dichroism*, [online]. Available from: <http://www.diamond.ac.uk/Beamlines/Surfaces-and-Interfaces/I06.html>.
- [13] BINNIG, G., H. ROHRER, Ch. GERBER and E. WEIBEL. Surface Studies by Scanning Tunneling Microscopy. *Phys. Rev. Lett.* 1982, vol. 49, pp. 57–61. Available from: doi:[10.1103/PhysRevLett.49.57](https://doi.org/10.1103/PhysRevLett.49.57).
- [14] LÜTH, H. *Solid Surfaces, Interfaces and Thin Films*. Springer, 2010.
- [15] BARDEEN, J. Tunnelling from a Many-Particle Point of View. *Phys. Rev. Lett.* 1961, vol. 6, pp. 57–59. Available from: doi:[10.1103/PhysRevLett.6.57](https://doi.org/10.1103/PhysRevLett.6.57).
- [16] VOIGTLÄNDER, B. *Scanning Probe Microscopy*. Springer, 2015.
- [17] SELLONI, A., P. CARNEVALI, E. TOSATTI and C. D. CHEN. Voltage-dependent scanning-tunneling microscopy of a crystal surface: Graphite. *Phys. Rev. B*. 1985, vol. 31, pp. 2602–2605. Available from: doi:[10.1103/PhysRevB.31.2602](https://doi.org/10.1103/PhysRevB.31.2602).
- [18] TERSOFF, J. and D. R. HAMANN. Theory and Application for the Scanning Tunneling Microscope. *Phys. Rev. Lett.* 1983, vol. 50, pp. 1998–2001. Available from: doi:[10.1103/PhysRevLett.50.1998](https://doi.org/10.1103/PhysRevLett.50.1998).
- [19] TERSOFF, J. and D. R. HAMANN. Theory of the scanning tunneling microscope. *Phys. Rev. B*. 1985, vol. 31, pp. 805–813. Available from: doi:[10.1103/PhysRevB.31.805](https://doi.org/10.1103/PhysRevB.31.805).
- [20] MIRONOV, V. L. *Fundamentals of the scanning probe microscopy*. Nizhniy Novgorod: Russian Academy of Science, 2004.
- [21] SCHAEFER, R. *Design and construction of a Scanning Tunneling Microscope* [online]. 1989. MA thesis. Carnegie Mellon University. Available from: <https://www.ece.cmu.edu/research/publications/1989/CMU-ECE-1989-028.pdf>.
- [22] UKRAINTSEV, Vladimir A. Data evaluation technique for electron-tunneling spectroscopy. *Phys. Rev. B*. 1996, vol. 53, pp. 11176–11185. Available from: doi:[10.1103/PhysRevB.53.11176](https://doi.org/10.1103/PhysRevB.53.11176).
- [23] STANFORD RESEARCH SYSTEMS, Inc. *Digital Lock-In Amplifiers* [online]. Available from: <http://www.thinksrs.com/downloads/PDFs/Catalog/SR810830c.pdf>.
- [24] STANFORD RESEARCH SYSTEMS, Inc. *About Lock-In Amplifiers* [online]. Available from: <http://www.thinksrs.com/downloads/PDFs/ApplicationNotes/AboutLIAs.pdf>.

- [25] KLEIN, J., A. LÉGER, M. BELIN, D. DÉFOURNEAU and M. J. L. SANGSTER. Inelastic-Electron-Tunneling Spectroscopy of Metal-Insulator-Metal Junctions. *Phys. Rev. B*. 1973, vol. 7, pp. 2336–2348. Available from: doi:10.1103/PhysRevB.7.2336.
- [26] ONNES, H.K. Further experiments with liquid helium. C. On the change of electric resistance of pure metals at very low temperatures etc. IV. The resistance of pure mercury at helium temperatures. *Commun. phys. Lab. Univ. Leiden*. 1911, vol. 120b.
- [27] ONNES, H.K. *Commun. phys. Lab. Univ. Leiden*. 1908, vol. 108.
- [28] MATTHIAS, B. T., T. H. GEBALLE and V. B. COMPTON. Superconductivity. *Rev. Mod. Phys.* 1963, vol. 35, pp. 1–22. Available from: doi:10.1103/RevModPhys.35.1.
- [29] MEISSNER, W. and R. OCHSENFELD. Ein neuer Effekt bei Eintritt der Supraleitfähigkeit. *Die Naturwissenschaften*. 1933, vol. 21.
- [30] LONDON, F. and H. LONDON. The Electromagnetic Equation of the Superconductor. *Proc. Roy. Soc.* 1935, vol. A149.
- [31] FOSSHEIM, K. and Sudbø. A. *Superconductivity: Physics and Applications*. John Wiley & Sons, Ltd, 2004.
- [32] BARDEEN, J., L. N. COOPER and J. R. SCHRIEFFER. Theory of Superconductivity. *Phys. Rev.* 1957, vol. 108, pp. 1175–1204. Available from: doi:10.1103/PhysRev.108.1175.
- [33] DELIN, K.A. and T.P. ORLANDO. *Superconductivity* [online]. Available from: [http://web.mit.edu/6.763/www/FT03/PSfiles/CH-117_\(KAD-TPO_revised\)_corrected_1.pdf](http://web.mit.edu/6.763/www/FT03/PSfiles/CH-117_(KAD-TPO_revised)_corrected_1.pdf).
- [34] SCHMIDT, V. V. *The Physics of Superconductors*. Springer, 1997.
- [35] DYNES, R. C., V. NARAYANAMURTI and J. P. GARNO. Direct Measurement of Quasiparticle-Lifetime Broadening in a Strong-Coupled Superconductor. *Phys. Rev. Lett.* 1978, vol. 41, pp. 1509–1512. Available from: doi:10.1103/PhysRevLett.41.1509.
- [36] SCIENTA OMICRON, GmbH. *LT-STM* [online]. 2016. Available from: <http://www.scientaomicron.com/en/products/low-temperature-spm/instrument-concepta>.
- [37] WOODCRAFT, Adam. *An introduction to cryogenics* [online]. Available from: <http://uk.lowtemp.org/1-Woodcraft.pdf>.
- [38] EKIN, Jack W. *Experimental techniques for low-temperature measurements*. Oxford University Press Inc., New York, 2006.
- [39] LAKE SHORE CRYOTRONICS, Inc. *Cryogenic wire specification* [online]. Available from: <http://www.lakeshore.com/products/cryogenic-accessories/wire/pages/Specifications.aspx>.
- [40] LAKE SHORE CRYOTRONICS, Inc. *Appendix I: Cryogenic Reference Tables* [online]. Available from: http://www.lakeshore.com/Documents/LSTC_appendixI_1.pdf.
- [41] FEMTO®, Messtechnik GmbH. *Variable Gain Low Noise Current Amplifier DLPCA-200* [online]. 2016. Available from: <http://www.femto.de/en/products/current-amplifiers/variable-gain-up-to-500-khz-dlpca.html>.

REFERENCES

- [42] SPECS, Zurich GmbH. *Nanonis SPM Control Systems* [online]. 2016. Available from: <http://www.specs-zurich.com/upload/cms/user/Nanonis1.pdf>.
- [43] BARTH, J. V., H. BRUNE, G. ERTL and R. J. BEHM. Scanning tunneling microscopy observations on the reconstructed Au(111) surface: Atomic structure, long-range superstructure, rotational domains, and surface defects. *Phys. Rev. B*. 1990, vol. 42, pp. 9307–9318. Available from: doi:10.1103/PhysRevB.42.9307.
- [44] WOODRUFF, D. P., W. A. ROYER and N. V. SMITH. Empty surface states, image states, and band edge on Au(111). *Phys. Rev. B*. 1986, vol. 34, pp. 764–767. Available from: doi:10.1103/PhysRevB.34.764.
- [45] CHEN, W., V. MADHAVAN, T. JAMNEALA and M. F. CROMMIE. Scanning Tunneling Microscopy Observation of an Electronic Superlattice at the Surface of Clean Gold. *Phys. Rev. Lett.* 1998, vol. 80, pp. 1469–1472. Available from: doi:10.1103/PhysRevLett.80.1469.
- [46] HASEGAWA, Y. and Ph. AVOURIS. Direct observation of standing wave formation at surface steps using scanning tunneling spectroscopy. *Phys. Rev. Lett.* 1993, vol. 71, pp. 1071–1074. Available from: doi:10.1103/PhysRevLett.71.1071.
- [47] PEARSON, W. B. and I. M. TEMPLETON. Superconducting Transition of Lead. *Phys. Rev.* 1958, vol. 109, pp. 1094–1094. Available from: doi:10.1103/PhysRev.109.1094.
- [48] FRANKE, K. J., G. SCHULZE and J. I. PASCUAL. Competition of Superconducting Phenomena and Kondo Screening at the Nanoscale. *Science*. 2011, vol. 332, no. 6032, pp. 940–944. Available from: doi:10.1126/science.1202204.
- [49] GUO, Yang, Yan-Feng ZHANG, Xin-Yu BAO, Tie-Zhu HAN, Zhe TANG, Li-Xin ZHANG, Wen-Guang ZHU, E. G. WANG, Qian NIU, Z. Q. QIU, Jin-Feng JIA, Zhong-Xian ZHAO and Qi-Kun XUE. Superconductivity Modulated by Quantum Size Effects. *Science*. 2004, vol. 306, pp. 1915–1917. Available from: doi:10.1126/science.1105130.
- [50] LEIJNSE, M. and K. FLENSBERG. Introduction to topological superconductivity and Majorana fermions. *Semiconductor Science and Technology* [online]. 2012, vol. 27, pp. 124003. Available from: <http://stacks.iop.org/0268-1242/27/i=12/a=124003>.
- [51] CORAUX, J., A. T. N'DIAYE, C. BUSSE and T. MICHELY. Structural Coherency of Graphene on Ir(111). *Nano Letters*. 2008, vol. 8, pp. 565–570. Available from: doi:10.1021/nl0728874.
- [52] BODE, M., S. HEINZE, A. KUBETZKA, O. PIETZSCH, M. HENNEFARTH, M. GETZLAFF, R. WIESENDANGER, X. NIE, G. BIHLMAYER and S. BLÜGEL. Structural, electronic, and magnetic properties of a Mn monolayer on W(110). *Phys. Rev. B*. 2002, vol. 66, pp. 014425. Available from: doi:10.1103/PhysRevB.66.014425.
- [53] LASSNER, E. and W.D. SCHUBERT. *Tungsten – Properties, Chemistry, Technology of the Element, Alloys, and Chemical Compounds*. Kluwer Academic/Plenum Publishers, 1999.
- [54] JOHNSON, K. E., R. J. WILSON and S. CHIANG. Effects of adsorption site and surface stress on ordered structures of oxygen adsorbed on W(110). *Phys. Rev. Lett.* 1993, vol. 71, pp. 1055–1058. Available from: doi:10.1103/PhysRevLett.71.1055.

- [55] BACHMANN, M., N. MEMMEL and E. BERTEL. Noble-metal nanostructures on carburized W(110). *Surface Science*. 2011, vol. 605, pp. 1263–1270. Available from: doi:http://dx.doi.org/10.1016/j.susc.2011.04.013.
- [56] OKAMOTO, H. V-W (Vanadium-Tungsten). *Journal of Phase Equilibria and Diffusion*. 2010, vol. 31, pp. 324–324. Available from: doi:10.1007/s11669-010-9703-y.
- [57] HAYENS, W.M. *CRC Handbook of Chemistry and Physics*. CRC Press: Boca Raton, 2015.
- [58] T N'DIAYE, A., J. CORAUX, T. N PLASA, C. BUSSE and T. MICHELY. Structure of epitaxial graphene on Ir(111). *New Journal of Physics* [online]. 2008, vol. 10, pp. 043033. Available from: <http://stacks.iop.org/1367-2630/10/i=4/a=043033>.
- [59] Von BERGMANN, K., S. HEINZE, M. BODE, G. BIHLMAYER, S. BLÜGEL and R. WIESENDANGER. Complex magnetism of the Fe monolayer on Ir(111). *New Journal of Physics* [online]. 2007, vol. 9, pp. 396. Available from: <http://stacks.iop.org/1367-2630/9/i=10/a=396>.
- [60] ROSE, James H., John R. SMITH, Francisco GUINEA and John FERRANTE. Universal features of the equation of state of metals. *Phys. Rev. B*. 1984, vol. 29, pp. 2963–2969. Available from: doi:10.1103/PhysRevB.29.2963.
- [61] KITTEL, Ch. *Introduction to Solid State Physics – 8th ed.* John Wiley & Sons, Ltd, 2005.
- [62] SURNEV, S., L. VITALI, M. G. RAMSEY, F. P. NETZER, G. KRESSE and J. HAFNER. Growth and structure of ultrathin vanadium oxide layers on Pd(111). *Phys. Rev. B*. 2000, vol. 61, pp. 13945–13954. Available from: doi:10.1103/PhysRevB.61.13945.
- [63] YOKOYAMA, T., T. NAKAGAWA and T. TAKAGI. Magnetic circular dichroism for surface and thin film magnetism: Measurement techniques and surface chemical applications. *International Reviews in Physical Chemistry*. 2008, vol. 27, pp. 449–505. Available from: doi:10.1080/01442350802127608.
- [64] STÖHR, J., H. A. PADMORE, S. ANDERS, T. STAMMLER and M. R. SCHEINFELN. Principles of X-Ray Magnetic Dichroism Spectromicroscopy. *Surface Review and Letters*. 1998, vol. 05. Available from: doi:10.1142/S0218625X98001638.
- [65] SCHÜTZ, G., W. WAGNER, W. WILHELM, P. KIENLE, R. ZELLER, R. FRAHM and G. MATERLIK. Absorption of circularly polarized x rays in iron. *Phys. Rev. Lett.* 1987, vol. 58, pp. 737–740. Available from: doi:10.1103/PhysRevLett.58.737.
- [66] Van der LAAN, Gerrit. Microscopic origin of magnetocrystalline anisotropy in transition metal thin films. *Journal of Physics: Condensed Matter* [online]. 1998, vol. 10, pp. 3239. Available from: <http://stacks.iop.org/0953-8984/10/i=14/a=012>.
- [67] NOVOSELOV, K. S., A. K. GEIM, S. V. MOROZOV, D. JIANG, Y. ZHANG, S. V. DUBONOS, I. V. GRIGORIEVA and A. A. FIRSOV. Electric Field Effect in Atomically Thin Carbon Films. *Science*. 2004, vol. 306, pp. 666–669. Available from: doi:10.1126/science.1102896.
- [68] MIWA, J. A., S. ULSTRUP, S. G. SØRENSEN, M. DENDZIK, A. G. ČABO, M. BIANCHI, J. V. LAURITSEN and P. HOFMANN. Electronic Structure of Epitaxial Single-Layer MoS₂. *Phys. Rev. Lett.* 2015, vol. 114, pp. 046802. Available from: doi:10.1103/PhysRevLett.114.046802.

REFERENCES

- [69] DENDZIK, M., M. MICHIARDI, Ch. SANDERS, M. BIANCHI, J. A. MIWA, S. S. GRØNBORG, J. V. LAURITSEN, A. BRUIX, B. HAMMER and P. HOFMANN. Growth and electronic structure of epitaxial single-layer WS₂ on Au(111). *Phys. Rev. B*. 2015, vol. 92, pp. 245442. Available from: doi:10.1103/PhysRevB.92.245442.
- [70] BRUIX, A., J. A. MIWA, N. HAUPTMANN, D. WEGNER, S. ULSTRUP, S. S. GRØNBORG, Ch. E. SANDERS, M. DENDZIK, A. GRUBI ŠI Č ČABO, M. BIANCHI, J. V. LAURITSEN, A. A. KHAJETOORIANS, B. HAMMER and P. HOFMANN. Single-layer MoS₂ on Au(111): Band gap renormalization and substrate interaction. *Phys. Rev. B*. 2016, vol. 93, pp. 165422. Available from: doi:10.1103/PhysRevB.93.165422.

List of used abbreviations

arb.u.	arbitrary unit
fcc/bcc	face-centred cubic/body-centred cubic
FFT	Fast Fourier Transformation
LN/LHe	Liquid Nitrogen/Liquid Helium
LDOS	Local Density of States
UHV	Ultra High Vacuum
LT-STM/S	Low Temperature Scanning Tunneling Microscopy/Spectroscopy
LEED	Low Energy Electron Diffraction
XPS	X-ray Photoelectron Spectroscopy
XAS	X-ray Absorption Spectroscopy
ARPES	Angle-resolved Photoelectron Spectroscopy
AC/DC	Alternating Current/Direct Current
XMCD	X-ray Circular Magnetic Dichroism
TMDC	Transition Metal Dichalcogenide
SOC	Spin Orbit Coupling
ML	Monolayer
MAE	Magnetic Anisotropy Energy
RCP/LCP	Right-Circularly-Polarized/Left-Circularly-Polarized